Optically Activated Gate Control for Power Electronics

Sudip K. Mazumder, *Senior Member, IEEE*, and Tirthajyoti Sarkar, *Member, IEEE*

***Abstract*—This paper outlines and demonstrates a novel optically activated gate control (OAGC) mechanism that can dynamically affect power-converter switching loss, dv/dt and di/dt stresses, and electromagnetic emission at the device level by controlling the switching dynamics of the power semiconductor device (PSD) via modulation of its excitation current using a GaAs-based optically triggered power transistor (OTPT). Further, due to conductivity modulation of the OTPT using direct photogeneration, the switching initiation delay using the OTPT-based OAGC approach is almost negligible, as compared to prevalent fiber-optics-based techniques for power electronics. Starting with a description of the basic mechanism of the OAGC and how it differs from other active-gate-control-based approaches, this paper outlines the implementation of the OAGC (including the design of the GaAs-based OTPT) and the mechanism for controlling the PSD turn-ON an turn-OFF dynamics by varying the optical intensity of the OTPT. Subsequently, the fundamental parameter, linking the control of the OTPT and its impact on the performance parameters of the power converter, is identified and the correlation is experimentally demonstrated. Finally, to address the mutually opposing dependence of switching loss, and dv/dt and di/dt stresses on the optical intensity of the OTPT, a joint optimization mechanism is outlined and its outcome is experimentally demonstrated.**

***Index Terms*—Active gate control (AGC), converter-performance parameters, delay, efficiency, electromagnetic (EM) noise, laser, optically activated gate control (OAGC), optically triggered power trasistor (OTPT), power electronics, power semiconductor device (PSD), stress, switching dynamics, switching loss.**

I. Introduction

NEXT-GENERATION power electronics are expected to encounter critical design challenges associated with electromagnetic (EM) emission and interference, switching loss, and dv/dt and di/dt stresses of power semiconductor devices (PSDs) [1]–[6].[1] There are several such emerging power electronics applications, which encounter one or more of the aforementioned problems, including EM aircraft launch system (EMALS) [7], fly-by-light (FBL) systems [8], [9], pulse-power and pulsed-load systems [10], [11], integrated starter and generator, and electromechanical actuator (EMA) motor drives [12], [13], flexible ac transmission systems (FACTSs) [1], and solid-state power substation (SSPS) [14]. The origin of these problems can be traced back to the switching dynamics of the PSDs. For instance, the EM-noise level of a power electronics system (PES) depends on the coupling between its parasitic inductances and capacitances, and the dv/dt and di/dt of the PSDs. The latter are governed by the rise and fall times of the PSD, which also affect the PSD stresses and its switching loss (and hence, the efficiency of the PES).

Active gate control (AGC) is a technique, which is traditionally applied in power electronics to modulate the switching dynamics of the PSDs, thereby controlling EM-noise generation, reducing the PSD dv/dt and di/dt stresses and switching losses [15]–[17]. Incorporation of AGC is illustrated in Fig. 1(a) and (b) for a single PSD even though, in general, the power stage may be composed of multiple PSDs. In these schemes, typically, the control stage generates one or more width-modulated logic signals, which are transmitted over electrical/optical links to the power stage to feed the gate drivers through optoisolators/photodetectors. The adaptive voltage-/current-excitation output of the gate driver, which modulates the PSD switching dynamics, is a function of the width-modulated signal and the intensity reference generated by the AGC.

The primary difference between the two schemes illustrated in Fig. 1(a) and (b) is the link between the control stage and the power stage. For the scheme in Fig. 1(a), this link is electrical, which is susceptible to external EM interference (EMI). This limitation is often overcome by replacing the electrical link with an optical link [18], [19], as illustrated in Fig. 1(b). It provides a reliable and inexpensive solution to conventional shielding, and reduces the overall weight and volume of the application (e.g., FBL system [9]). However, the photodetector, which acts only as a logic signal detector, cannot modulate the switching dynamics of the PSD.

Further, notwithstanding the differences between the two schemes, an additional delay is incurred in the optoisolator and the photodetector stages. Additionally, an AGC scheme, referred in Fig. 1(a) and (b), is designed to modulate the switching dynamics of an individual PSD of the power stage, and is typically not an integral part of the conventional converter control design. Because AGC modulates the PSD switching dynamics, which, in turn, affects the EM-noise emission, dv/dt and di/dt stresses, and power-conversion efficiency of a converter (*referred from*

Manuscript received June 1, 2009; revised August 7, 2009; accepted September 30, 2009. Date of current version October 5, 2011. This work is supported in parts by the awards received by Prof. S. K. Mazumder from the Office of Naval Research (ONR) and the National Science Foundation (NSF). The content of this paper is covered by [1] S. K. Mazumder and T. Sarkar, "Optically-triggered power system and devices," USPTO Patent Application Number US 2009/0283664 A1, Nov. 9, 2009 (provisional patent filed on Jun. 2007). [2] S.K. Mazumder and T. Sarkar, "Optically-triggered multi-stage power system and devices," USPTO Patent Application Number US 2009/00226967, Jan. 29, 2009 (provisional patent filed on May 2, 2006). Addendum application with regard to patent application cited in " [1]." Recommended for publication by Associate Editor R.-L. Lin.

S. K. Mazumder is with the Electrical and Computer Engineering, University of Illinois, Chicago, IL 60607 USA (e-mail: mazumder@ece.uic.edu).

T. Sarkar is with the Fairchild Semiconductor, Pune, Maharastra 411006 India (e-mail: tirthajyoti.sarkar@fairchildsemi.com).

Color versions of one or more of the figures in this paper are available online at http://ieeexplore.ieee.org.

Digital Object Identifier 10.1109/TPEL.2009.2034856

[1]A brief overview on some of the issues outlined in this paper has been provided in Refs. [2], [9], and [33].

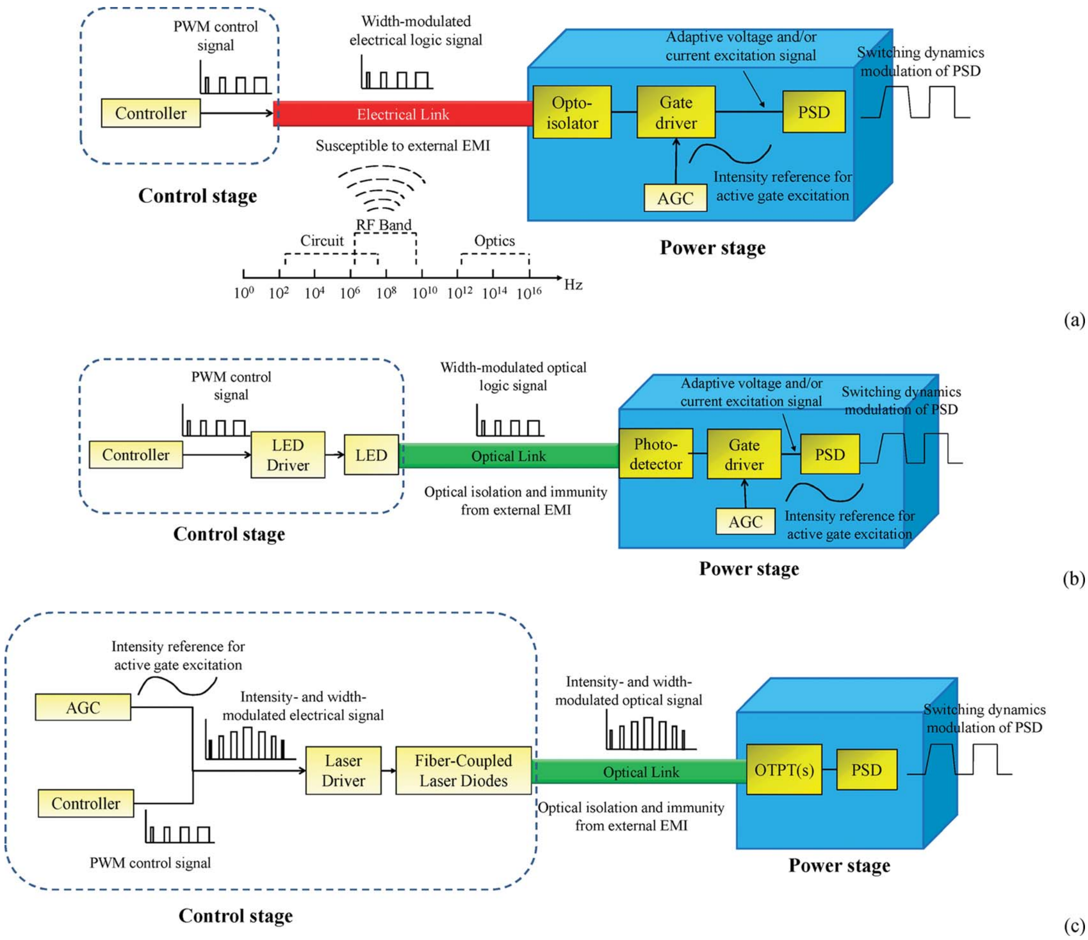

Fig. 1. Illustrations of AGC in conventional power electronics application with (a) electrical and (b) optical links. (c) Illustration of an OAGC-based power-conversion system.

here on as converter-performance parameters), it is logical to consider integrating AGC with conventional converter control.

Such a novel integration, along with optical isolation, which provides the immunity from external EMI and back-propagating power-stage voltage and current transients [9], [19], [20], is illustrated in Fig. 1(c). It is referred in this paper as the *optically activated gate control* (*OAGC*) scheme. In the OAGC scheme, the outputs of the PWM controller and the AGC are merged to generate a pulsewidth- and pulse-amplitude-modulated signal, which is fed to a laser via a laser driver. Subsequently, width- and intensity-modulated optical output of a laser activates an optically triggered power transistor (OTPT), which, unlike a photodetector illustrated in Fig. 1(b), integrates two functionalities: light-to-electrical conversion and control of the PSD gate excitation. Because of this direct integration using OTPT, the time delay between control initiation and PSD activation is significantly reduced as compared to the schemes outlined in Fig. 1(a) and (b).

Rest of the paper is as follows. Section II describes the OAGC scheme along with its implementation issues, and outlines the impact of OAGC on the PSD switching dynamics and converter-performance parameters. In Section III, the principle of operation of the GaAs-based OTPT along with its design and optical-interface issues are discussed. In Section IV, first, steady-state and switching characterization results of the OTPT are shown. Subsequently, OTPT-based modulation of the switching dynamics of a PSD is demonstrated. Finally, the effect of OTPT-based OAGC on converter-performance parameters is experimentally demonstrated and a methodology to achieve an optimal tradeoff among these parameters is outlined.

II. OAGC Concept

In this section, the operating principle of the OAGC, and its impact on the PSD switching parameters and converter-performance parameters are outlined. For illustration of the concept, a power MOSFET is chosen as the PSD (although the same concept can be extended to other types of PSDs, as demonstrated in Section IV).

A. Principle of Operation and Implementation Schemes

Conventionally, the AGC schemes focus on the modulation of the switching dynamics of a power MOSFET by controlling the gate-voltage dynamics. One of the most critical phases of the gate-voltage waveform of a power MOSFET is the Miller plateau, which denotes the relatively flat portion of the power MOSFET gate-to-source voltage waveform. In this phase, most of the current supplied by the gate driver charges/discharges the effective MOSFET gate-to-drain capacitance (which is amplified in magnitude compared to its nominal steady-state value

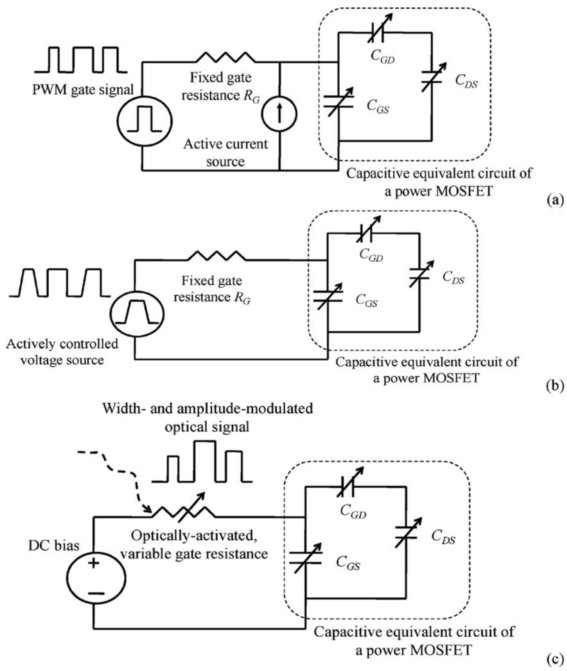

Fig. 2. (a) Active current injection. (b) Active-voltage-slope-based AGCs. (c) Optically activated variable-gate-resistance-based OAGC.

due to the Miller effect) and the power-MOSFET gate-to-source voltage does not increase in magnitude. Further, most of the switching loss occurs in this phase because the drain-to-source voltage and the drain-to-source current undergo their sharpest transition during this phase. Therefore, the primary focus of many conventional AGC schemes has been the reduction of this Miller plateau width for mitigating the switching loss. Fig. 2 shows the broad categories of conventional AGC schemes actively controlling the profile of the injected gate current [see Fig. 2(a)], and the shape and slope of the applied gate voltage [see Fig. 2(b)].

In contrast, in the OAGC scheme, as illustrated in Fig. 2(c), the PSD switching-dynamics modulation is achieved by varying the effective resistance between the dc bias and the gate of the power MOSFET. The information encoded in the optical signal serves two purposes: 1) the pulsewidth information determines when the power MOSFET is turned on or turned off, while 2) the pulse-amplitude information enables modulation of the gate resistance, thereby modulating the charging/discharging rate of the power MOSFET input capacitances (C_{GS} and C_{GD}) and the switching dynamics of the power MOSFET. The mechanism for implementing the OAGC scheme is illustrated in Fig. 3(a) using the principal optically activated element (OTPT) that serves as the variable gate resistance.

Each OTPT (i.e., ON-OTPT or OFF-OTPT) is activated in a complimentary manner using the ON-laser or the OFF-laser output within a certain wavelength, while the variable intensity of the optical signal modulates the conductivity of the OTPT by photogeneration–recombination process. The ON-laser or the OFF-laser is fed by a laser driver, which produces amplitude-modulated current-drive signals to produce the corresponding amplitude-modulated optical output. In the illuminated state, photogeneration and subsequent transistor action enhances the conductivity of the ON-OTPT, thereby reducing its ON-resistance. (During the same time, the OFF-OTPT stays in the nonconducting and high-resistivity mode.) Subsequently, a gate-excitation current from the V_{Bias} flows through the ON-OTPT and charges the power-MOSFET gate up to the level of V_{Bias} with respect to V_{Ref}. In a complimentary manner, when the OFF-OTPT is illuminated, it acts as a discharging element and pulls down the gate potential of the power MOSFET close to the V_{Ref} level, thereby turning the power MOSFET OFF. During this phase, the ON-OTPT is in OFF state.

While the configuration in Fig. 3(a) can control both the turn-ON and the turn-OFF dynamics of the power MOSFET, Fig. 3(b) and (c) represent special cases of OAGC implementation that control, respectively, only the turn-ON and the turn-OFF dynamics of the power MOSFET. In Fig. 3(b) or (c), the OTPT controlled with variable-intensity optical signal is placed in the charging/discharging path, while the discharging/charging path consists of a fixed resistor (or an OTPT activated with optical signal of fixed intensity). The physical resistor eliminates the need for an additional OTPT, and its optical source and driver, but results in a higher power dissipation. The value of the fixed resistor cannot be chosen too high because it increases the charging/discharging time of the power MOSFET; it cannot be too low because it leads to enhanced power dissipation.

Although the OAGC needs a filtered and isolated dc logic bias, it may not be affected by a radiated EMI because of higher power level (compared to the time-varying control signal) and zero fundamental frequency of the bias. Alternatively, an all-optical approach may employ a photocell-based dc logic supply.

B. PSD Switching-Dynamics Modulation Using OAGC

Fig. 4 illustrates the effect of OAGC on the PSD switching dynamics by showing the correlation between the optical input to the OTPT and the OTPT ON-resistance, and gate-to-source and drain-to-source voltages of a power MOSFET. Optical signals of two different intensity levels are shown. A higher intensity of the optical signal results in an enhanced photogeneration of electron–hole carriers inside the OTPT. Therefore, the steady-state ON-resistance of the OTPT goes down with increasing optical intensity [21], which leads to faster charging/discharging of the input capacitance of the power MOSFET. Therefore, the gate-to-source voltage of the power MOSFET reaches the threshold voltage in a shorter amount of time or the Miller plateau shrinks due to faster charging of the gate-to-drain capacitance of the power MOSFET. While the rise times of the ON-OTPT and OFF-OTPT have a direct impact only on the PSD [i.e., power MOSFET in Fig. 3(a)] turn-ON and turn-OFF delays ($t_{\mathrm{ON\text{-}delay,PSD}}$ and $t_{\mathrm{OFF\text{-}delay,PSD}}$), the ON-resistance of the OTPTs affect the PSD delays, and the rise and fall times ($t_{\mathrm{rise,PSD}}$ and $t_{\mathrm{fall,PSD}}$), as shown in Fig. 4. A higher optical intensity for the OTPT results in a smaller rise time due to faster rate of photogeneration inside the OTPT [22], and therefore, leads to a smaller delay.

An analysis of the switching-dynamics modulation, based on the circuit shown in Fig. 3(a) with grounded reference point (i.e., $V_{\mathrm{Ref}} = 0$), is outlined next. Because the ON-OTPT controls the charging of the power-MOSFET gate, this charging

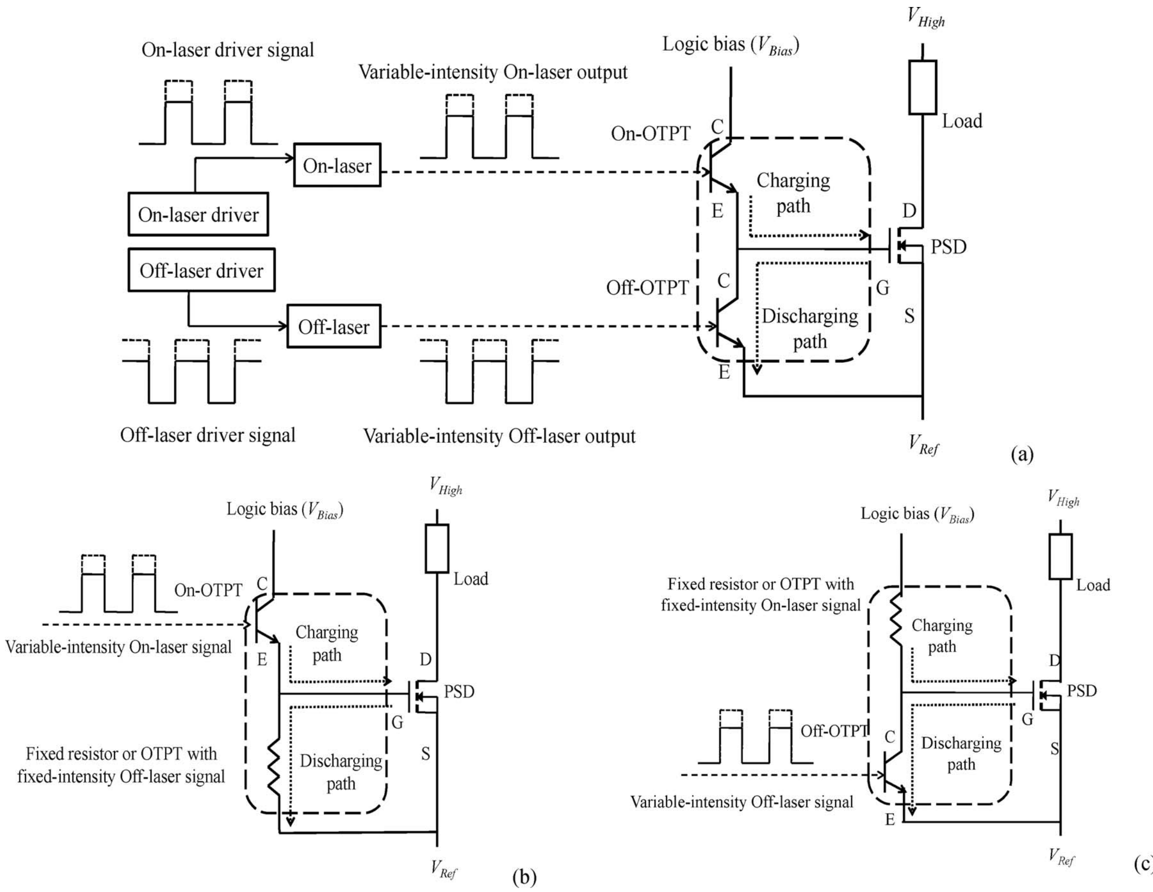

Fig. 3. Illustration of the OAGC schemes using (a) turn-ON and turn-OFF controllability, (b) only turn-ON controllability, and (c) only turn-OFF controllability. Scheme in (a) uses two OTPTs and two variable-intensity pulsating optical signals. For (b) and (c), the discharging/charging path consists of either a fixed physical resistor or an OTPT activated by a fixed-intensity optical signal. Hybrid packaging realizations of (a) and (b) are shown in Fig. 14 (c) and (d), respectively. Such a package is composed of active devices and if a physical resistor is used then it is not part of the package. Electrical terminals are indicated by the symbols G, D, S, C, and E that represent gate, drain, source, collector, and emitter, respectively.

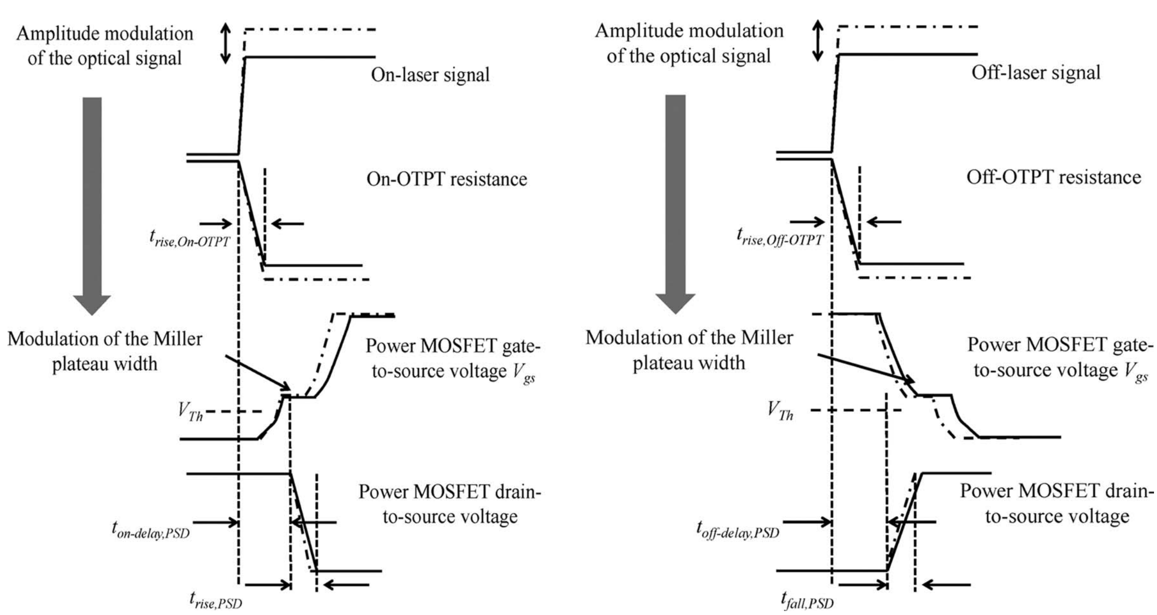

Fig. 4. Illustration of the OTPT-based modulation of the PSD switching dynamics with amplitude modulation of the optical signal.

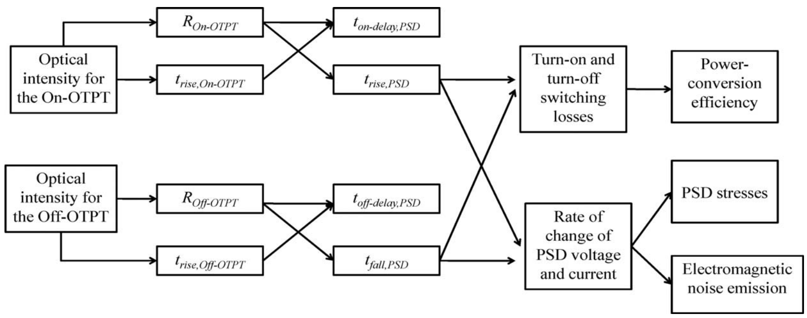

Fig. 5. Illustration showing the functional relationship between the converter-performance parameters and the OTPT optical intensity.

dynamics (under the assumption that the change in the OFF-to-ON-state optical intensity is instantaneous, which also implies that the optical-intensity-dependent impedance of the ON-OTPT or $f_1(P_{\text{ON-OTPT}})$, which is described in Appendix I, is a constant) is given using the following relation [22]:

$$C_{\mathrm{iss}} \frac{dV_{\mathrm{gs}}}{dt} = \frac{V_{\mathrm{Bias}} - V_{\mathrm{gs}}}{f_1(P_{\text{ON-OTPT}})} \Rightarrow V_{\mathrm{gs}}(t) = V_{\mathrm{Bias}}\left(1 - e^{-t/f_1(P_{\text{ON-OTPT}})C_{\mathrm{iss}}}\right) \quad (1)$$

where $_{\mathrm{OTPT}}$ is the intensity of the optical input activating the ON-OTPT, C_{iss} is the effective input capacitance, and V_{gs} is the gate-to-source voltage of the power MOSFET. The power MOSFET begins conducting when V_{gs} reaches the threshold voltage V_{Th}. Effectively, $t_{\text{ON-delay,PSD}}$ is the sum of the time needed for charging C_{iss} to V_{Th} and the rise time of the ON-OTPT or $t_{\text{rise,ON-OTPT}}$ (that is related to $P_{\text{ON-OTPT}}$ via the function $f_2\,(P_{\text{ON-OTPT}})$ that is described in Appendix I). This yields [22]

$$t_{\text{ON-delay,PSD}} = f_2\,(P_{\text{ON-OTPT}}) + C_{\mathrm{iss}} f_1\,(P_{\text{ON-OTPT}}) \ln\left(\frac{V_{\mathrm{Bias}}}{V_{\mathrm{Bias}} - V_{\mathrm{Th}}}\right). \quad (2)$$

Now, assuming that the generic forms of $f_1(\cdot)$ and $f_2(\cdot)$ are applicable for both ON-OTPT and OFF-OTPT, and noting the complementary switching of the OTPTs, $t_{\text{OFF-delay,PSD}}$, $t_{\text{rise,PSD}}$, and $t_{\text{fall,PSD}}$ can be expressed as follows [22]:

$$t_{\text{OFF-delay,PSD}} = f_2(P_{\text{OFF-OTPT}}) + C_{\mathrm{iss}} f_1(P_{\text{OFF-OTPT}}) \ln\left(\frac{V_{\mathrm{Bias}}}{V_{\mathrm{Th}}}\right) \quad (3)$$

$$t_{\text{rise,PSD}} = C_{\mathrm{iss}} f_1(P_{\text{ON-OTPT}}) \ln\left(\frac{V_{\mathrm{Bias}}}{V_{\mathrm{Bias}} - (V_{\mathrm{Th}} + (I_{\mathrm{in}}/g_{\mathrm{fs}}))}\right) \quad (4)$$

$$t_{\text{fall,PSD}} = C_{\mathrm{iss}} f_1(P_{\text{OFF-OTPT}}) \ln\left(\frac{V_{\mathrm{Th}} + (I_{\mathrm{in}}/g_{\mathrm{fs}})}{V_{\mathrm{Th}}}\right) \quad (5)$$

where I_{in} is the steady-state current flowing through the power MOSFET and g_{fs} is its forward transconductance.

C. Modulation and Optimization of Converter-Performance Parameters Using OAGC

In Fig. 5, a functional relationship between the intensity of the input optical signals for the ON-OTPT and OFF-OTPT (used, respectively, for controlling the turn-ON and turn-OFF dynamics of the PSD) and the converter-performance parameters is explained. The optical intensity of each OTPT controls its ON-resistance and rise or fall time, which have a direct impact on the turn-ON and turn-OFF delays of the PSD, and its rise and fall times. This, in turn, controls the switching losses of the PSD and its dv/dt and di/dt, which directly influence converter-performance parameters, as outlined next using some case illustrations.

1) Illustrations of the Effect of OTPT Optical Intensity on Converter-Performance Parameters: The power-conversion efficiency of a hard-switched buck converter, illustrated in Fig. 25, is approximated by

$$\eta = \frac{P_{\mathrm{load}}}{P_{\mathrm{load}} + L_{\mathrm{lump}} + L_{\mathrm{SW}}} \quad (6)$$

where P_{load} is the output power, L_{SW} is the switching loss of the power MOSFET, and L_{lump} is the net sum of other losses (for instance, conduction and switching losses of the diode, parasitic losses, and conduction loss of the power MOSFET). Analytical expression for L_{SW} is approximated, using [23], and (4) and (5), to be

$$\begin{aligned} L_{\mathrm{SW}} &= f_{\mathrm{SW}} \frac{V_{\mathrm{in}} I_{\mathrm{in}}}{2} \left[t_{\text{rise,PSD}} + t_{\text{fall,PSD}}\right] \\ &= f_{\mathrm{SW}} \frac{V_{\mathrm{in}} I_{\mathrm{in}}}{2} C_{\mathrm{iss}} \\ &\quad \times \left[f_1(P_{\text{ON-OTPT}}) \ln\left(\frac{V_{\mathrm{Bias}}}{V_{\mathrm{Bias}} - (V_{\mathrm{Th}} + (I_{\mathrm{in}}/g_{\mathrm{fs}}))}\right) \right. \\ &\quad \left. + f_1(P_{\text{OFF-OTPT}}) \ln\left(\frac{V_{\mathrm{Th}} + (I_{\mathrm{in}}/g_{\mathrm{fs}})}{V_{\mathrm{Th}}}\right) \right] \end{aligned} \quad (7)$$

where f_{SW} is the switching frequency and V_{in} is the steady-state voltage across the power MOSFET. Using the expression of L_{SW} from (7) in (6), one obtains, (8) as shown at the bottom of this page

$$\eta = \frac{P_{\mathrm{load}}}{P_{\mathrm{load}} + L_{\mathrm{lump}} + f_{\mathrm{SW}} \frac{V_{\mathrm{in}} I_{\mathrm{in}}}{2} \left[\lambda_1 C_{\mathrm{iss}} f_1\,(P_{\text{ON-OTPT}}) + \lambda_2 C_{\mathrm{iss}} f_1\,(P_{\text{OFF-OTPT}})\right]} \quad (8)$$

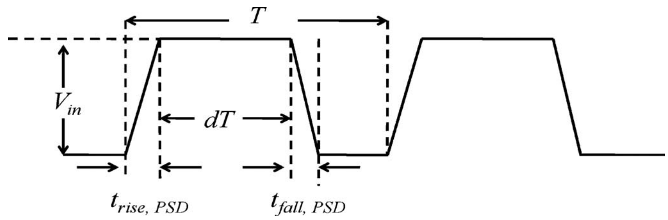

Fig. 6. Waveform of the trapezoidal switching voltage across a PSD for frequency-spectrum analysis. Symbols T and d represent switching period and duty cycle, respectively.

where

$$\lambda_1 = \ln\left(\frac{V_{\rm Bias}}{V_{\rm Bias} - (V_{\rm Th} + I_{\rm in}/g_{\rm fs})}\right) \quad \lambda_2 = \ln\left(\frac{V_{\rm Th} + I_{\rm in}/g_{\rm fs}}{V_{\rm Th}}\right). \tag{9}$$

In (9), $V_{\rm Bias}$ and $V_{\rm Th}$ are referenced with respect to the source potential of the power MOSFET. It is noted from (7) and (8) that switching loss (or power-conversion efficiency) is a function of the optical intensities of the ON-OTPT and OFF-OTPT and, following (A1), decreases (or increases) with increasing OTPT optical intensity.

Furthermore, for the buck converter, the dv/dt and the di/dt stresses of the power MOSFET during turn-ON and turn-OFF transients can be written (using linear approximation) as

$$\left.\frac{dv}{dt}\right|_{\rm ON} = \frac{V_{\rm in}}{\lambda_1 C_{\rm iss} f_1\left(P_{\text{ON-OTPT}}\right)}$$
$$\left.\frac{dv}{dt}\right|_{\rm OFF} = \frac{V_{\rm in}}{\lambda_2 C_{\rm iss} f_1\left(P_{\text{OFF-OTPT}}\right)} \tag{10a}$$
$$\left.\frac{di}{dt}\right|_{\rm ON} = \frac{I_{\rm in}}{\lambda_1 C_{\rm iss} f_1\left(P_{\text{ON-OTPT}}\right)}$$
$$\left.\frac{di}{dt}\right|_{\rm OFF} = \frac{I_{\rm in}}{\lambda_2 C_{\rm iss} f_1\left(P_{\text{OFF-OTPT}}\right)}. \tag{10b}$$

It is evident from (10) that the dv/dt and the di/dt stresses can be modulated by varying optical intensities of the ON-OTPT and OFF-OTPT, and following (A1), the stresses increase with increasing OTPT optical intensity.

Analyses of the harmonic amplitude and the spectral envelope of the frequency spectrum of a switching waveform have appeared in the literature [24]–[27]. However, most of these analyses assume equal rise and fall times. A more general and practical case for analyzing a switching waveform with unequal rise and fall times (as observed in most of the commonly used PSDs) is needed. In Fig. 6, such a waveform is illustrated. The relationship between the magnitude of the harmonics and the OTPT optical intensity is explained through the PSD rise and fall times. Following the derivation in Appendix II, the magnitude of the nth harmonic is given by

$$|A_n| = |a_n - jb_n| = \sqrt{a_n^2 + b_n^2}$$
$$= \sqrt{g_1^2(t_{\rm rise,PSD}, t_{\rm fall,PSD}) + g_2^2(t_{\rm rise,PSD}, t_{\rm fall,PSD})} \tag{11}$$

where the forms of functions $g_1(\cdot)$ and $g_2(\cdot)$ are given by (A8a) and (A8b) in Appendix II, respectively. Equation (11) implies that *the magnitude of A_n is a function of the OTPT optical intensity and it increases with increasing OTPT optical intensity according to (A8).*

2) OTPT Optical Intensity for Optimal Tradeoff Among Switching Loss and PSD dv/dt and di/dt Stresses: Equations (7), (8), (10), and (11) indicate that with increasing OTPT optical intensity, while power-conversion efficiency increases (since switching loss decreases), the dv/dt- and di/dt-related PSD stresses and EM noise also increase. Although variation in the optical intensity only affects $L_{\rm SW}$, it may be difficult to experimentally measure $L_{\rm SW}$ of a converter directly. On the other hand, from the ratio of the output and input power of a converter, power-conversion efficiency can be measured in a straightforward manner. Now, the total loss $L_{\rm total}$ (i.e., the sum of $L_{\rm lump}$ and $L_{\rm SW}$) is a function of optical power because $L_{\rm SW}$ decreases with optical power and $L_{\rm lump}$ remains constant. To obtain a tradeoff among $L_{\rm total}$, and dv/dt and di/dt stresses, an optimization framework is outlined in (15) with the assumption that ON-OTPT and OFF-OTPT *are activated with equal optical intensity*, i.e., $P_{\text{ON-OTPT}} = P_{\text{OFF-OTPT}} = P_{\rm OTPT}$. Under this assumption, $L_{\rm total}$ can be calculated [using (6)] as follows:

$$L_{\rm total}\left(P_{\rm OTPT}\right) = L_{\rm SW} + L_{\rm lump} = \left(\frac{1}{\eta} - 1\right) P_{\rm load}. \tag{12}$$

The functional dependency of $L_{\rm total}$ on $P_{\rm OTPT}$ is established by (8). The expressions for dv/dt and di/dt for turn-ON and turn-OFF, following (10), can be rewritten as follows:

$$\left.\frac{dv}{dt}\right|_{\rm total}\left(P_{\rm OTPT}\right) = \frac{V_{\rm in}}{\lambda_1 C_{\rm iss} f_1(P_{\rm OTPT})} + \frac{V_{\rm in}}{\lambda_2 C_{\rm iss} f_1(P_{\rm OTPT})} \tag{13a}$$

$$\left.\frac{di}{dt}\right|_{\rm total}\left(P_{\rm OTPT}\right) = \frac{I_{\rm in}}{\lambda_1 C_{\rm iss} f_1(P_{\rm OTPT})} + \frac{I_{\rm in}}{\lambda_2 C_{\rm iss} f_1(P_{\rm OTPT})}. \tag{13b}$$

Now, $L_{\rm total}$ is expressed in terms of watts, and dv/dt and di/dt are expressed in terms of volts per microseconds or amperes per microseconds. These quantities differ in units and magnitudes, and therefore, need to be normalized with respect to a uniform scale to be used in the objective function. Maximum values of $L_{\rm total}$, and dv/dt and di/dt (denoted by $L_{\rm total}^{\rm max}$, $dv/dt|_{\rm max}$, and $di/dt|_{\rm max}$) are taken as the normalization factors, and the resultant nominal functions are given by

$$L_{\rm total}^{\rm nom}\left(P_{\rm OTPT}\right) = \frac{L_{\rm total}\left(P_{\rm OTPT}\right)}{L_{\rm total}^{\rm max}} \tag{14a}$$

$$\left.\frac{dv}{dt}\right|_{\rm nom}\left(P_{\rm OTPT}\right) = \frac{dv/dt|_{\rm total}\left(P_{\rm OTPT}\right)}{dv/dt|_{\rm max}} \tag{14b}$$

$$\left.\frac{di}{dt}\right|_{\rm nom}\left(P_{\rm OTPT}\right) = \frac{di/dt|_{\rm total}\left(P_{\rm OTPT}\right)}{di/dt|_{\rm max}}. \tag{14c}$$

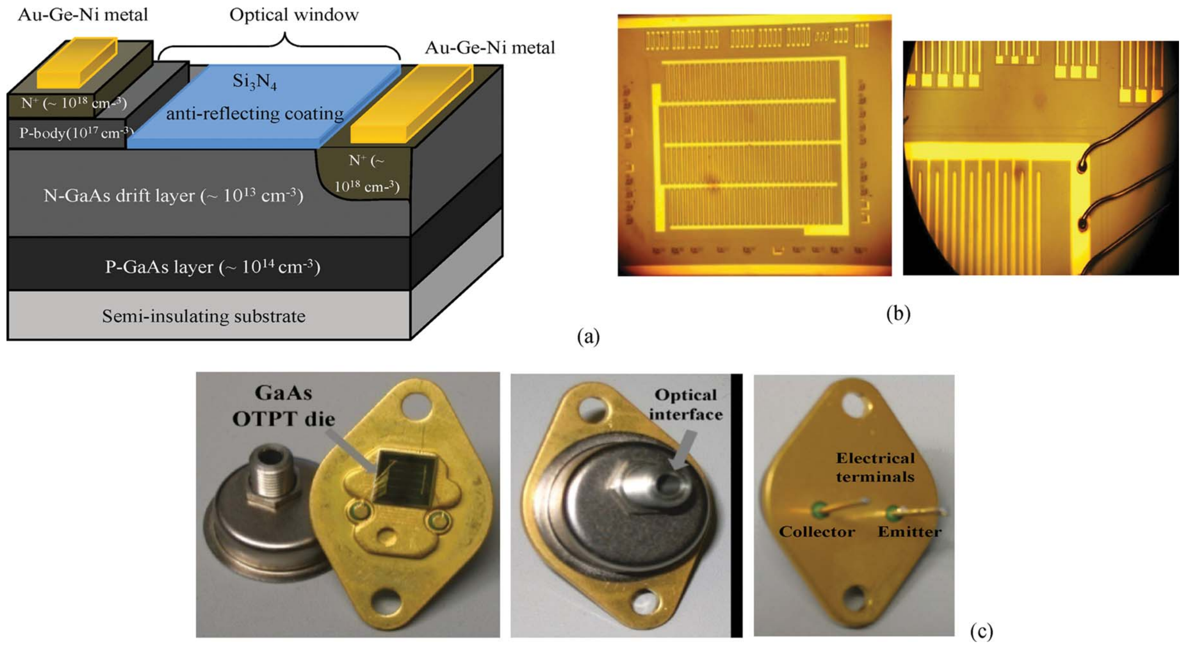

Fig. 7. (a) Device structure of the OTPT. (b) Micrograph of a prototype OTPT and its die wire bonding. (c) Packaged realization of the OTPT.

The optimization problem using the objective function $J(P_{\mathrm{OTPT}})$ is defined as follows.

Minimize

$$J(P_{\mathrm{OTPT}}) = \alpha_1 L_{\mathrm{total}}^{\mathrm{nom}}(P_{\mathrm{OTPT}}) + \alpha_2 \left.\frac{dv}{dt}\right|_{\mathrm{nom}} (P_{\mathrm{OTPT}}) + \alpha_3 \left.\frac{di}{dt}\right|_{\mathrm{nom}} (P_{\mathrm{OTPT}}) \tag{15}$$

subject to

$$\begin{pmatrix} L_{\mathrm{total}}^{\mathrm{nom}} \\ \left.\dfrac{dv}{dt}\right|_{\mathrm{nom}} \\ \left.\dfrac{di}{dt}\right|_{\mathrm{nom}} \end{pmatrix} = H\left(P_{\mathrm{OTPT}}\right)$$

$$P_{\min} < P_{\mathrm{OTPT}} < P_{\max}$$

$$\alpha_1 + \alpha_2 + \alpha_3 = 1 \quad \text{and} \quad \alpha_1 \geq 0, \quad \alpha_2 \geq 0, \quad \alpha_3 \geq 0$$

where α_1, α_2, and α_3 signify the relative degrees of priority of switching loss, dv/dt, and di/dt in the objective function. Proper selection of these weights is important as relative levels of the priority from a system standpoint can vary. The vector function $H\left(P_{\mathrm{OTPT}}\right)$ maps the dependence of $L_{\mathrm{total}}^{\mathrm{nom}}$, $dv/dt|_{\mathrm{nom}}$ and $di/dt|_{\mathrm{nom}}$ on P_{OTPT}, and these dependencies are theoretically described, respectively, by (8), (9), (12), and (14a); (A1), (10), (13a), and (14b); and (A1), (10), (13b), and (14c). For a specific application, an alternate way to determine $H\left(P_{\mathrm{OTPT}}\right)$ is via empirical mapping, which has been adopted in this paper and illustrated in Section IV. Now, it follows from the *extreme-value theorem* [28] that

1) there may exist a global minima for $J(P_{\mathrm{OTPT}})$ at the *stationary point* P_{OTPT}^* where the first derivative of $J(P_{\mathrm{OTPT}})$ with respect to P_{OTPT} vanishes, i.e.,

$$\left.\frac{d\left(J\left(P_{\mathrm{OTPT}}\right)\right)}{dP_{\mathrm{OTPT}}}\right|_{P_{\mathrm{OTPT}} = P_{\mathrm{OTPT}}^*} = 0 \tag{16}$$

2) the minimum point may lie at the boundary of the range of P_{OTPT} (i.e., either at $P_{\min}$ or $P_{\max}$), i.e., the minimum value of the objective function corresponds to the lowest or highest value of the attainable P_{OTPT}.

III. GaAs-Based OTPT for OAGC: Design, Optical Interface, and Hybrid Packaging With PSD

This section describes the OTPT, which is the principal component of the OAGC scheme. Because the OTPT is different from a commercially available photodetector (generally used in fiber-optic-based power electronics), basic structure, operational mechanism, and design issues of the OTPT are described with particular regard to its conductivity modulation.

A. Structure and Operation

The OTPT is shown in Fig. 7 with structural, micrograph, and packaged representations. GaAs is chosen as the base material because it features high optical efficiency (with optical absorption coefficient of 10^4 cm^{-1} near 800 nm wavelength range), high electron mobility, and low-carrier-recombination lifetime. These properties of GaAs [29] enable the OTPT to attain rapid turn-ON and turn-OFF capabilities (thereby minimizing the delay between the optical excitation of the OTPT and the actuation of the PSD) and good optical responsivity (thereby minimizing optical-triggering power requirement). The OTPT has an emitter

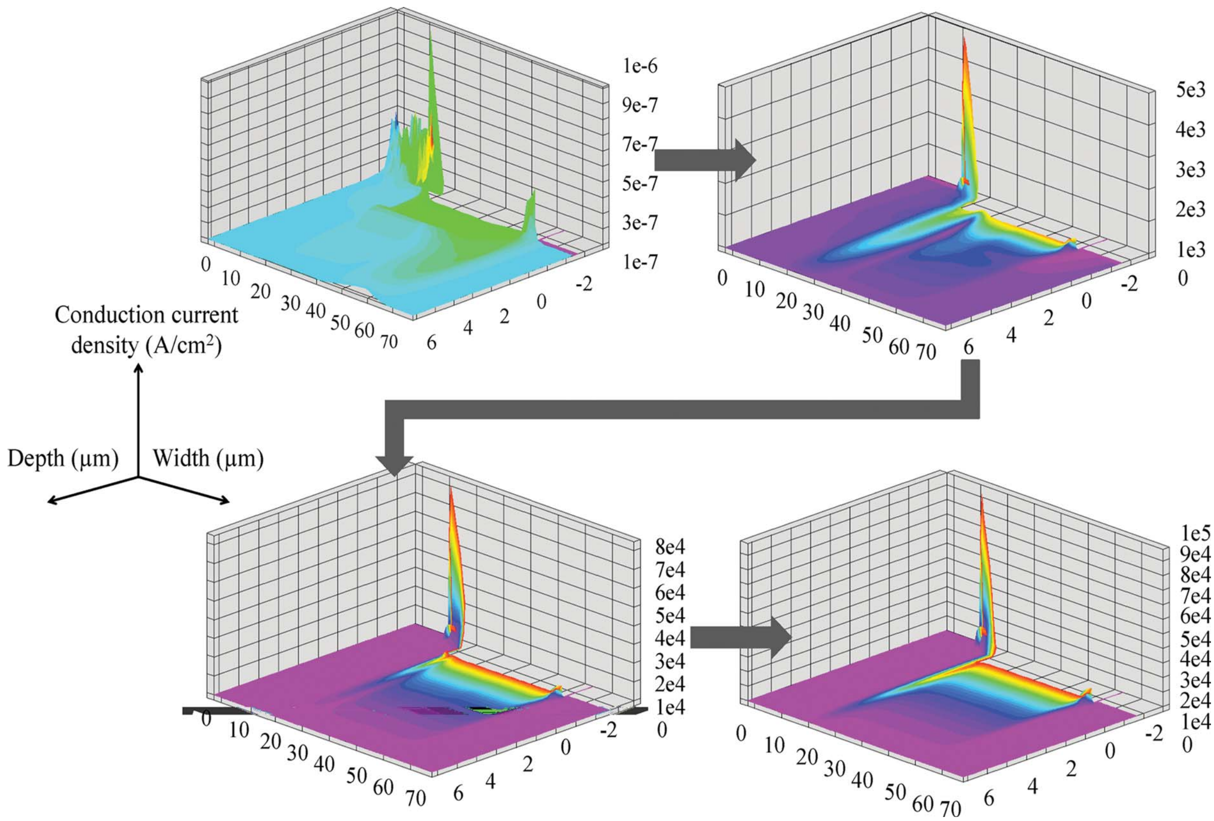

Fig. 8. Transition of the OTPT from the OFF-state to the ON-state when activated by the optical signal. A multifold increase in the magnitude of the current density due to increased photogenerated carrier density is observed. (a)–(d) Current-density distribution inside OTPT at four equally spaced time instants.

and a collector. Shallow low-energy implantation with Si atoms is done to realize high-doped N^+ emitter region. Au–Ge–Ni alloyed metal layers, deposited by E-beam evaporation, form the electrodes for the collector and the emitter. The optical window is defined by the Si_3N_4 antireflecting (AR) coating deposited using plasma-enhanced CVD (PECVD) technique. The N^+ collector, P-body, and N- and P-GaAs epitaxial layers are grown using metalloorganic CVD (MOCVD) technique.

In the OFF-state, voltage across the OTPT is supported by the reverse-biased p-n junction between the P-body and N-GaAs drift regions. When the activating beam falls on the OTPT, it is absorbed in the optical window region, thereby generating electron–hole plasma by photogeneration. This plasma, mobilized by the electric field, is then attracted by the collector and emitter electrodes, and constitutes electron and hole currents, thereby taking the OTPT to the ON-state. If the optical signal is sustained, conductivity remains high, and the switch remains closed. When the optical signal shuts OFF, the carriers recombine, and the OTPT goes back to its high-resistivity blocking state. The degree of conductivity modulation (by the photogenerated carriers) varies with the optical power. Fig. 8 shows the conduction-current density inside the OTPT at four equally spaced time frames during turn-ON transient. The vertical axis represents the conduction current density, which undergoes large change from Fig. 8(a) to (b) (during ON-state to OFF-state transition) and from Fig. 8(b) to (c) (during conductivity modulation); however, the change is relatively small from Fig. 8(c) to (d). Fig. 8 denotes that, with varying optical power, the OTPT initially undergoes a large change in its resistance, and then the resistance is modulated with increasing optical power. However, for progressively higher optical power, the OTPT resistance variation enters a flatter and saturated regime.

B. Structural Design Issues for Conductivity Modulation

The principal function of the OTPT in the OAGC scheme is to modulate the switching dynamics of the PSD. Varying optical intensity produces varying degree of conductivity modulation in the OTPT, which leads to switching-dynamics modulation of the PSD. If a small degree of optical-intensity variation can lead to large variation in the OTPT conductivity (or the ON-resistance in an inverse manner), then the overall requirement on the optical-triggering power will be less demanding. *Therefore, the design of the OTPT and its optical interface needs to produce large variation in conductivity with reduced optical power*.

The doping levels and thicknesses of the epitaxial layers have been designed such that the total positive charge contributed by P-GaAs layer nullifies the total negative charge contributed by the N-GaAs drift layer [9]. This results in a uniform rectangular electric field, which enables reduced effective distance between collector and emitter electrodes of the unit cell of the OTPT, and yields higher optical gain because photogenerated carriers travel

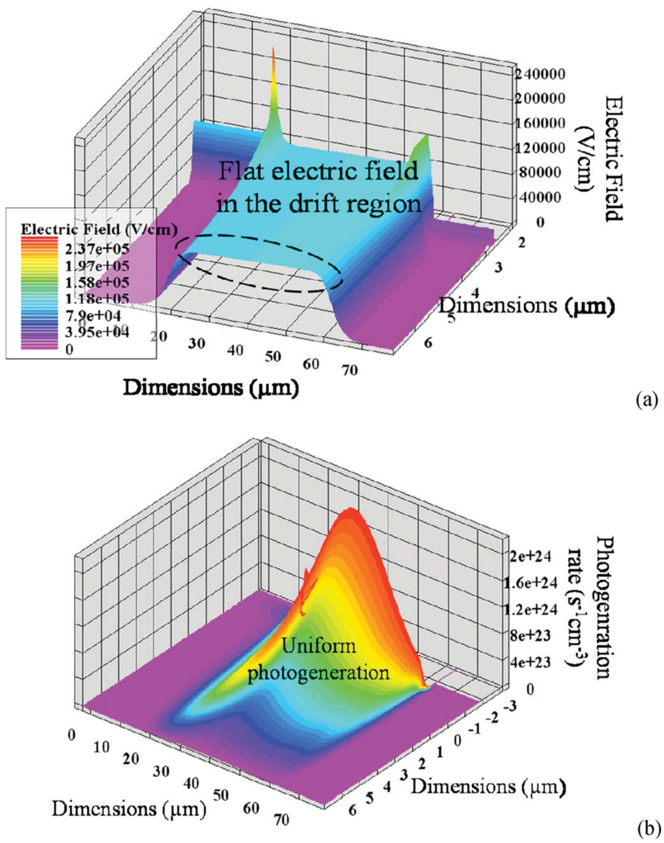

Fig. 9. (a) 3-D view of the electric field distribution inside the OTPT at the instant of breakdown. (b) 3-D view of the uniform photogeneration rate inside the OTPT.

less distance inside N-drift region. Also, a rectangular electric field [see Fig. 9(a)] mobilizes the photogenerated carriers in a uniform manner, as demonstrated in Fig. 9(b). Moreover, the quantum efficiency and the switching speed of the OTPT depend strongly on the minority-carrier-recombination lifetime in the P-body region. A higher doping of the P-body results in a shorter lifetime, which ensures faster turn-OFF due to rapid recombination when the light shuts off, but it also leads to a lower device gain because photogenerated carriers recombine easily and have less chance of contributing toward conductivity modulation. Fig. 10 shows comparative pictures of recombination rate and conduction-current density for two OTPTs with identical dimensions, but different P-body doping density.

Particular thickness and refractive index of the Si_3N_4 film is designed so that minimum light is reflected from the front surface. Reflectivity as a function of varying Si_3N_4 layer coating thickness and different refractive indexes are calculated, and the result is plotted in Fig. 11. A suitable thickness (300 nm) has been chosen from this plot to achieve minimum reflectivity.

C. Issues for the Optical Interface and Packaging of the OTPT for Conductivity Modulation

Typically, the output beam from laser diode has elliptical shape with approximately Gaussian power distribution [30]. Simulations show that the optical triggering beam should be as circularly uniform as possible. Nonuniform illumination may result in uneven current distribution inside the bulk of the device and even leads to low optical gain that yields lower quantum efficiency. Fig. 12 shows comparative pictures of the identical OTPT illuminated by two optical beams having different wavefront shapes in terms of the Gaussian spread. The lower spread of optical beam leads to localized photogeneration in Fig 12(a), yielding far lower conduction current density.

The wavelength of the incident optical beam is a critical design parameter, as it strongly influences the reflectivity and optical absorption depth [29] inside the OTPT, which affect the overall photogeneration rate, and hence, the degree of conductivity modulation. Fig. 13 shows photogeneration rate inside OTPT for 400- and 800-nm wavelengths of the optical beam and corresponding modulation in the electrical field for identical optical intensity. Due to lower reflectivity and larger depth of absorption, an 800-nm wavelength beam produces higher modulation of the electric field to mobilize the photogenerated carriers more intensely for conduction.

The packaged hybrid integration is demonstrated in Fig. 14. Dies of Si-based power MOSFET, Si-based insulated-gate bipolar transistor (IGBT), SiC-based vertical junction FET (VJFET), and SiC-based DMOSFET are obtained from International Rectifier, SiCED AG, and Cree, Inc., respectively, and are copackaged with the GaAs-based OTPT die. The aim of such hybrid packaging is to reduce the interconnect length to minimize the parasitic impedance between the OTPT(s) and the PSD due to the interconnects. Furthermore, the optical fiber can be terminated into a single hybrid package, thereby enhancing the immunity of the PSD, as well as the OTPT-PSD interconnects to external EM noise. Key issues for such hybrid packaging are the mutual placement of the OTPT and the PSD dies. The PSD die is a vertical device with bond pads on both sides of the die, whereas the bond pads of the OTPT are on the top surface of the die and the backside of the OTPT is not metalized because of its lateral device structure. Therefore, the bottom bond pad of the PSD die is soldered onto a conductive metal pad from which bond wires are brought out for external electrical connections. Furthermore, both the OTPT and the PSD dies need to dissipate heat through the package floor while in operation. However, the lateral OTPT and the vertical PSD dies cannot be directly attached to the package floor as their backside cannot be at the same electrical potential. Dies, therefore, are pasted on to a thermally conductive, but electrically insulating, die attach material (beryllium oxide), which helps conduction of heat, but provides necessary electrical isolation.

It is noteworthy that, for the development of first generation OTPT, the die size was chosen approximately 7 mm × 7 mm. This was done to ensure low resistance, good heat dissipation capability, and uniform illumination of light on the die from a vertical optical-fiber termination. The layout of the OTPT is of interdigitated type with the distance between individual pair of fingers depending on the voltage rating of the device, and the length and width of the fingers depending on the current rating. Therefore, by adjusting the number of fingers and their 2-D distribution, the die size of the OTPT can be reduced significantly. This is expected to reduce the cost per unit die for the OTPT.

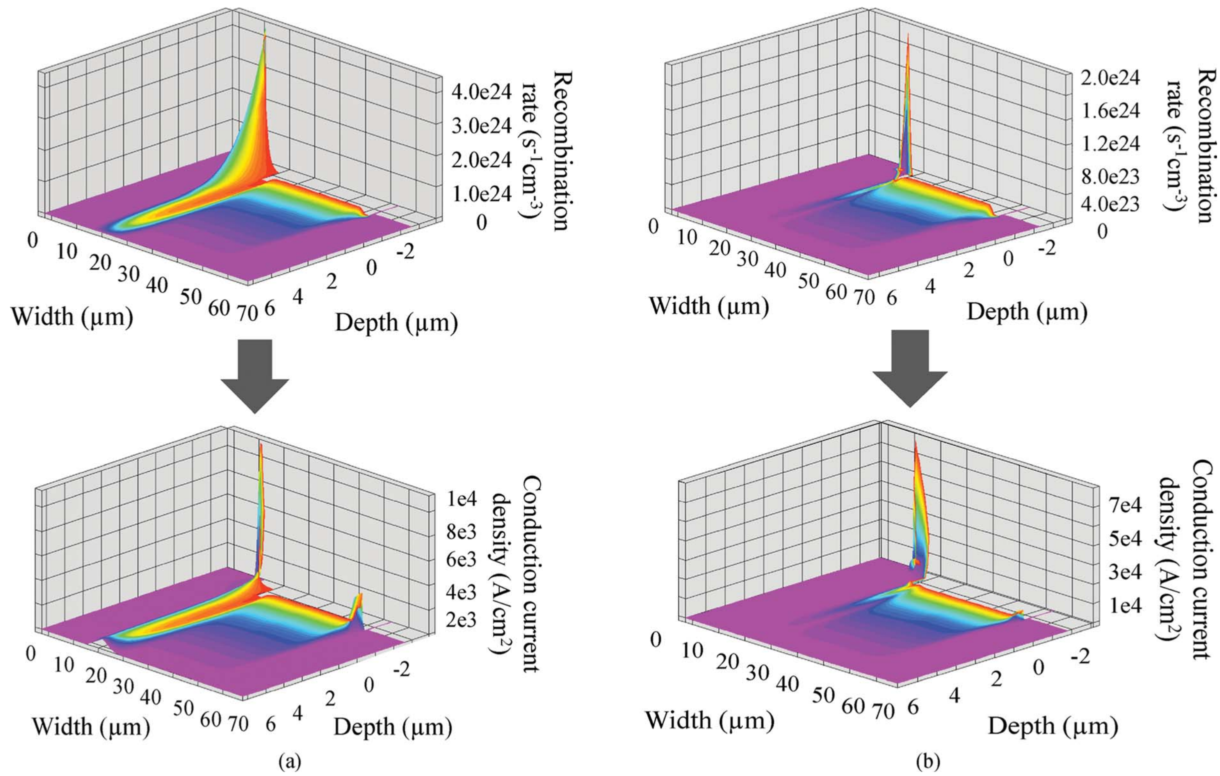

Fig. 10. Comparative plots of photogeneration and conduction current density of OTPTs with (a) higher doped P-body and (b) lower doped P-body. This suggests that the P-body doping density should not be made too high because it results in enhanced recombination leading to poor conductivity modulation.

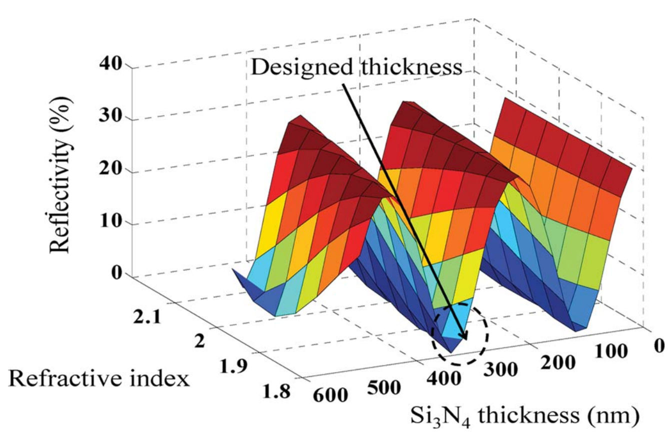

Fig. 11. Reflectivity as a function of AR coating thickness and refractive index. Lower reflectivity yields higher optical absorption leading to better conductivity modulation, and therefore, 300 nm thickness is chosen for the design.

IV. Experimental Results and Discussions

A. Steady-State and Switching Characterizations of the GaAs-Based OTPT

In this section, steady-state I–V characteristics and switching dynamics characterization of the OTPT are presented. *Optical intensity is defined to be the optical power per unit area.* For optical-intensity-modulation experimentations, one key assumption, which holds for all the experimental results in this paper, is made. Further, it is assumed that the optical illumination is uniform and the area of illumination remains identical (because identical laser, laser-to-fiber coupler, optical fiber, and fiber-to-OTPT interface are used) for all experimental conditions. Experimental results, therefore, feature optical power (which can be estimated with greater accuracy based on the measurement of laser-drive current and the laser-diode characteristics) as the independent variable. Optical test setup details are provided in Table I.

Dark resistivity is an important property of an optically triggered device, as it determines the leakage current under nonilluminated condition. For a large-peak-current-rated device, where the active area of the individual die is quite large, leakage current must be kept small to prevent static loss in the triggering circuit. Dark resistivity of the GaAs-based OTPT is measured under nonilluminated condition using a Tektronix 371 A curve tracer and the result is shown in Fig. 15. Less than 1-μA steady-state current flows through the OTPT when a steady-state 50 V current is applied across the OTPT. Therefore, the dark resistance can be approximated to be $\approx$50 V/1 μA $=$ 50 MΩ.

Next, the characterizations of the single OTPT for the nominal switching operation are carried out and the switching parameters are measured. The resistive load circuit is shown in Fig. 16. For power electronic applications, one of the most important characteristics is the ability of the OTPT to follow a triggering optical signal of variable pulsewidth. Pulse-following capability of the OTPT is tested at switching frequencies of 20 and 80 kHz by programming the duty cycle of the optical signal over a broad range. The linear relationship between the duty cycles of

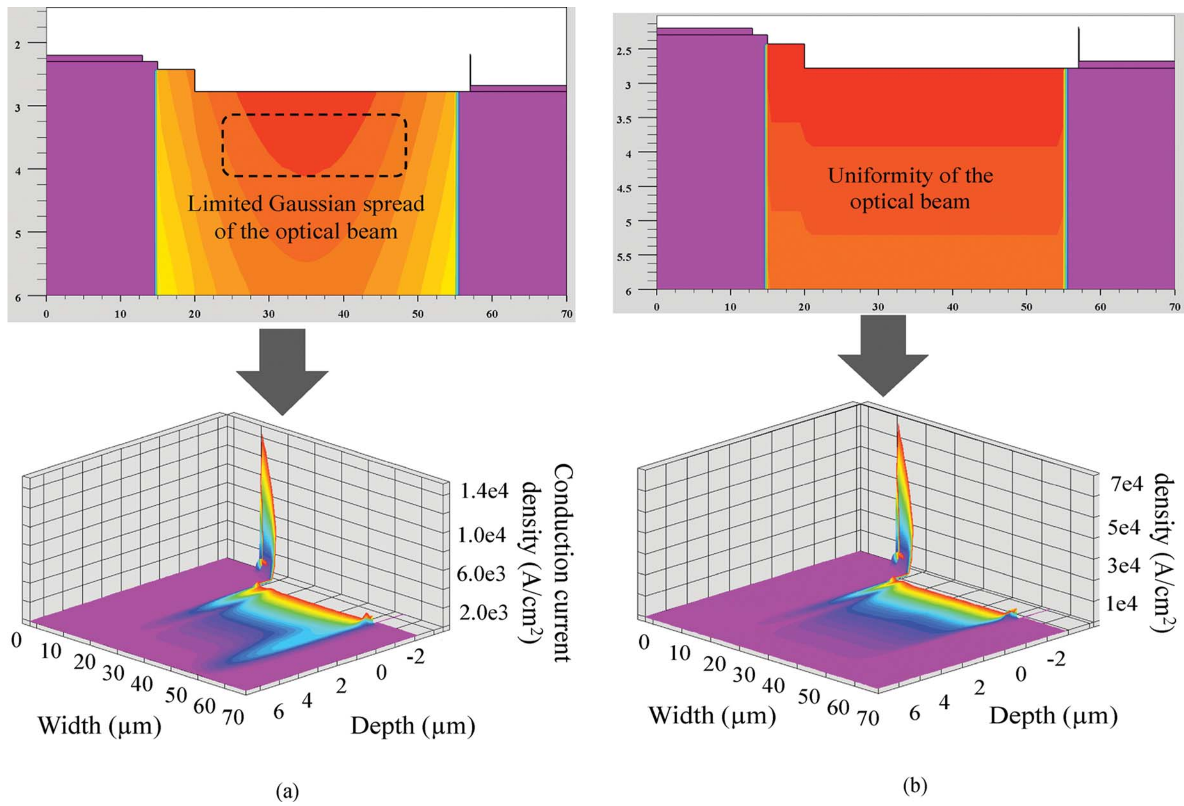

Fig. 12. Comparative plots of photogeneration rate and corresponding conduction current density using (a) optical beam with Gaussian wavefront of small spread and (b) uniform optical beam. This suggests that a uniform optical wavefront is better suited for OTPT conductivity modulation.

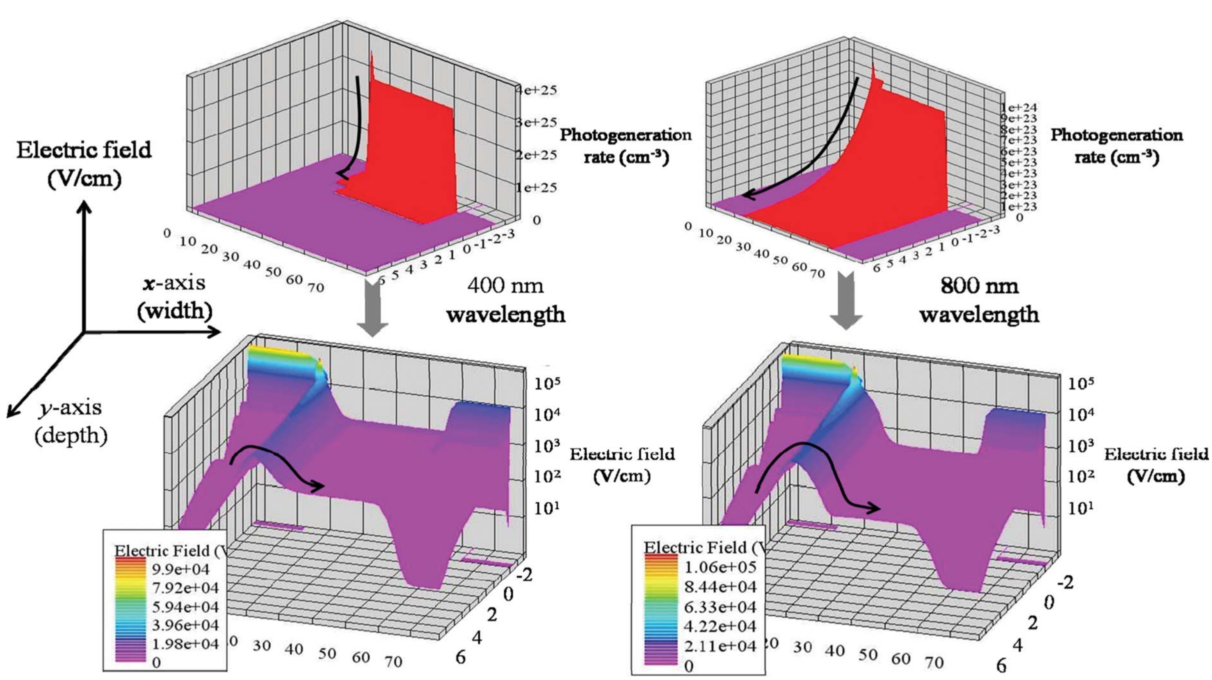

Fig. 13. Comparative plots of photogeneration rate and corresponding electric field using optical beam of (left) 400 nm and (right) 800 nm wavelength for the identical optical intensity. This suggests that an optical beam with 800 nm wavelength produces larger electric field modulation.

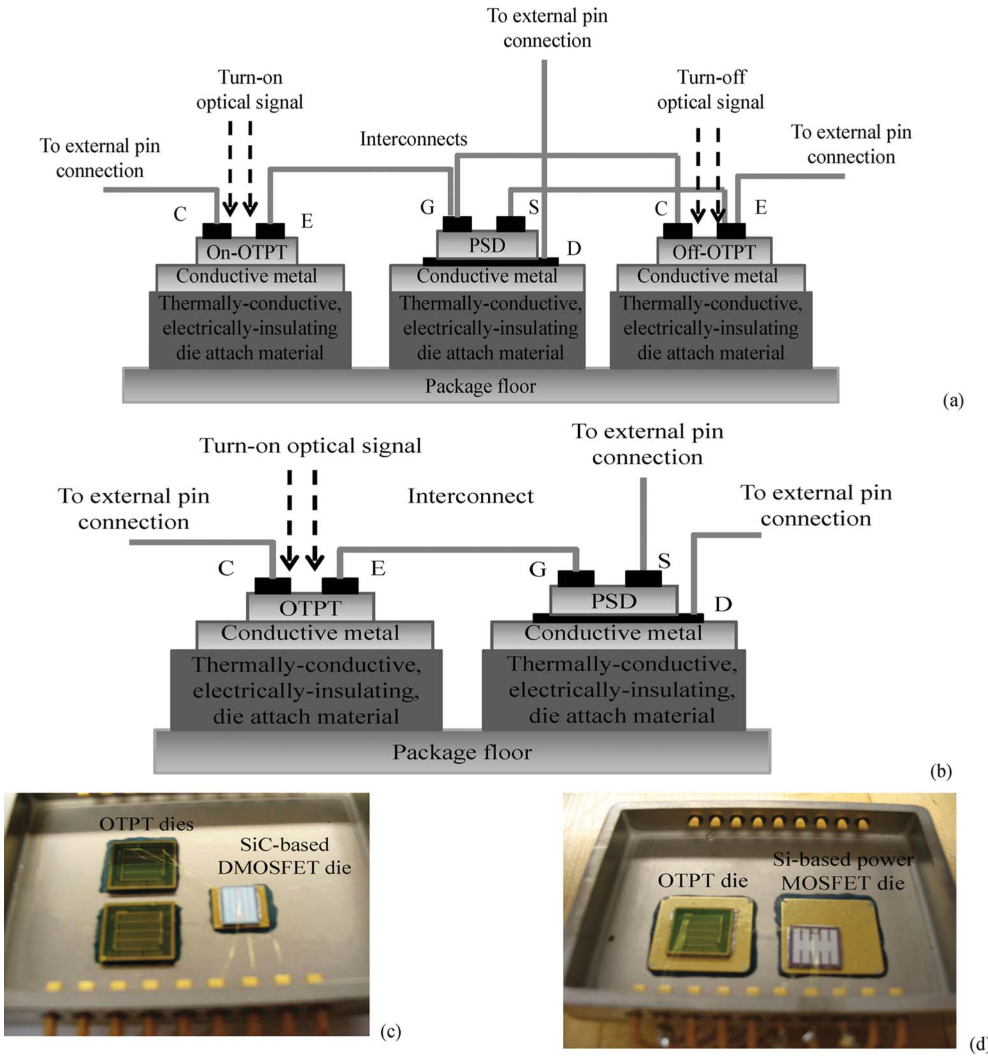

Fig. 14. Hybrid packaging scheme with (a) two OTPTs coupled to a vertical PSD die and (b) single OTPT coupled to a vertical PSD die corresponding to Fig. 3(a) and (b), respectively. Corresponding prototype packages are shown in (c) and (d) where the PSD dies are (c) SiC-based DMOSFET and (d) Si-based power MOSFET, respectively. Electrical terminals are indicated by the symbols G, D, S, C, and E that represent gate, drain, source, collector, and emitter, respectively.

TABLE I
DETAILS OF THE LASER, LASER DRIVER, OPTICAL FIBER, AND OPTICAL INTERFACE USED FOR EXPERIMENTAL MEASUREMENT

Laser	FAP-600	Fiber characteristics	600 µm core diameter, multi-mode	Laser-to-fiber coupler	SMA-900
Laser driver	PCX-7410	Fiber numerical aperture	0.37	Fiber-to-OTPT coupler	SMA-900

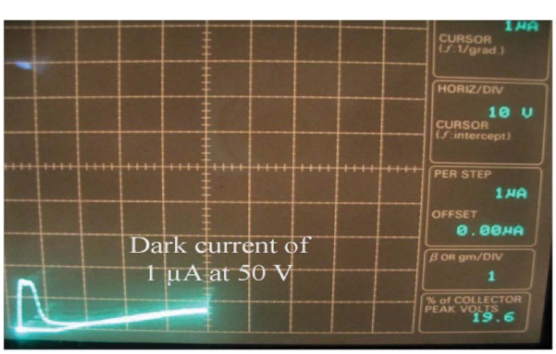

Fig. 15. Conduction characteristic of the OTPT without illumination. Dark resistance is obtained to be approximately 50 MΩ.

the optical signal and the OTPT output voltage signal is shown in Fig. 17. It is noted that the maximum switching frequency and the duty cycle of the OTPT is determined by the laser driver, and the type and rating of the PSD. For instance, in our experiments, the output of the laser driver could only achieve a maximum of 95% duty cycle and 100 kHz frequency. However, the fast temporal response of the OTPT (as evident in Fig. 19) clearly indicates the ability of the OTPT to follow signals with higher repletion rate.

Modulation of the PSD switching dynamics strongly depends on the variation of the OTPT ON-state resistance. The OTPT ON-state resistance is measured by a point-by-point method using the resistive load circuit of Fig. 16. In this method, voltage drop

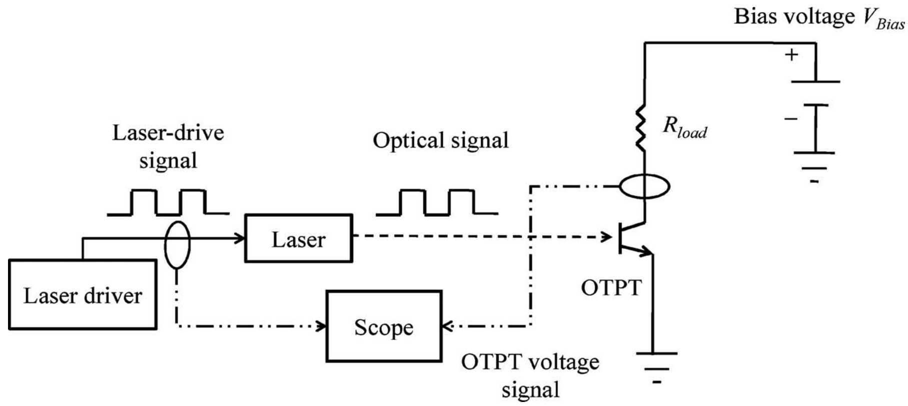

Fig. 16. Switching characterization setup for the OTPT.

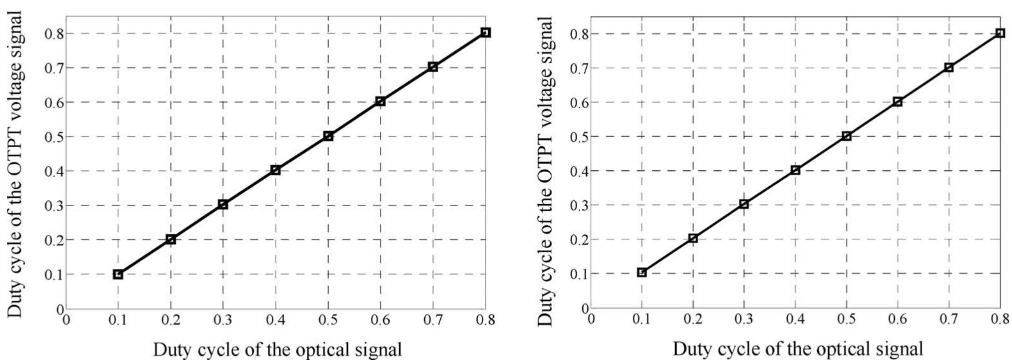

Fig. 17. Experimentally measured linearity of the duty cycle of the OTPT voltage signal and the optical signal over a wide range of duty cycles (0.1–0.8) for (a) 20 kHz and (b) 80 kHz, and under the following conditions: $V_{\rm Bias} = 60$ V, $R_{\rm load} = 1000\ \Omega$, and optical power = 1 W.

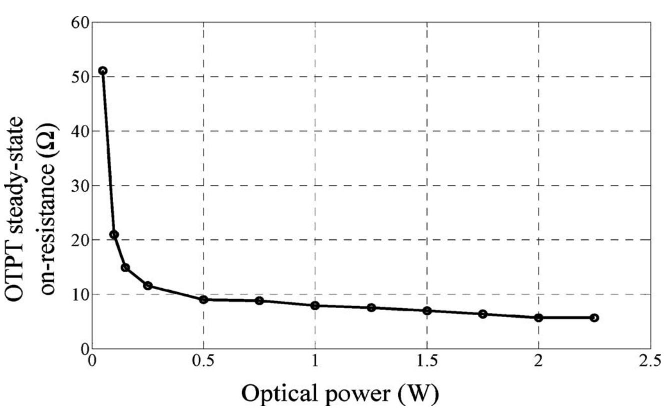

Fig. 18. Experimentally measured modulation of the OTPT steady-state ON-resistance with varying optical power under the following conditions: $V_{\rm Bias} = 10$ V, $R_{\rm load} = 50\ \Omega$, frequency = 5 kHz, and duty cycle = 50%.

across the OTPT during steady-state conduction is measured for different optical power levels. Resistance values are extracted from these data points, and they are plotted to show the variation (see Fig. 18). Low bias voltage of 10 V is used for this experimentation so as to achieve high level of resolution in the measurement of the ON-state voltage drop of the OTPT. Switching frequency is also lowered to 5 kHz so as to allow the OTPT to remain in the steady-state conduction mode for a larger time. Fig. 18 shows a sharp drop in the ON-resistance with variation in optical power, and then enters a relatively flat saturation region. This behavior is expected from the theoretical analysis [21] and (A1), which outline the nonlinear relation between the OTPT ON-resistance and the intensity of its optical signal.

Next, snapshots of the turn-ON and turn-OFF dynamics of the OTPT are shown in Fig. 19. Turn-ON and turn-OFF delays are measured as the difference between the time instants of the initiation of the laser-drive signal and initiation of the change in the OTPT voltage. Rise and fall times are defined as the time taken to change the OTPT voltage from 10% to 90% (or *vice versa*) of its steady-state value.

B. Characterizations of the OAGC-Based PSD Switching Dynamics

In this section, the results on the switching-dynamics modulation of the PSD are presented. The circuit arrangement is similar to Fig. 3(a) and the PSD is chosen to be a CoolMOS power MOSFET (Infineon part number 47N50). First, the modulation of the Miller plateau width with increasing OTPT optical intensity is demonstrated. Fig. 20(a) shows how an increment in the optical power leads to a reduction in the Miller plateau width. Fig. 20(b) shows multiple gate-to-source voltage

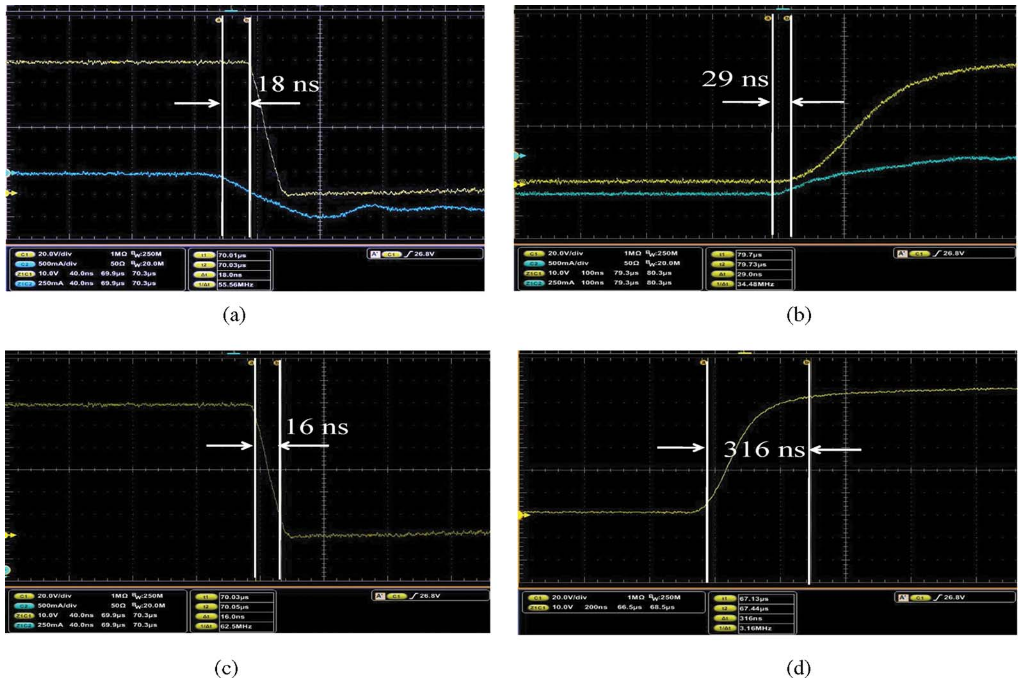

Fig. 19. Snapshot of the (a) turn-ON delay, (b) turn-OFF delay, (c) rise time, and (d) fall time of the OTPT under the following conditions: $V_{\rm Bias} = 60$ V, $R_{\rm load} = 1000\ \Omega$, frequency $= 50$ kHz, duty cycle $= 50\%$, and optical power $= 0.5$ W. Scale for the vertical axis is 10 V/div, while for the horizontal axes are: (a) 40 ns/div, (b) 100 ns/div, (c) 40 ns/div, and (d) 200 ns/div, respectively. For (a) and (b), the top trace is the voltage across the OTPT and the bottom trace is the output current signal of the laser driver. The laser-driver current signal is measured through an internal current monitor of the laser driver and is of negative polarity. The threshold current, at which the lasing starts, is ~6 A.

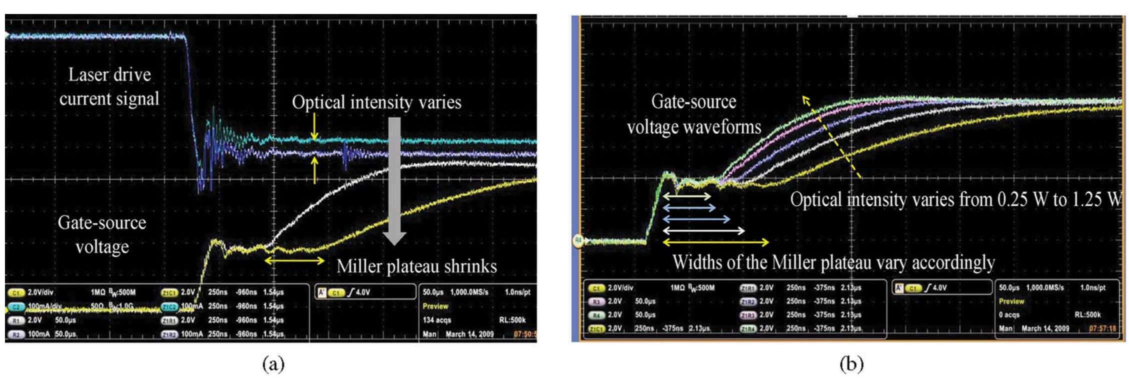

Fig. 20. Modulation of the Miller plateau width in the gate-voltage dynamics of the power MOSFET (CoolMOS 47N50) with varying optical power levels under the following conditions: $V_{\rm Bias} = 12$ V, $V_{\rm High} = 50$ V, $R_{\rm load} = 40\ \Omega$, and frequency $= 30$ kHz.

(corresponding to multiple optical intensity levels) superimposed onto each other, which clearly illustrates the variation of the Miller plateau width as the optical power changes.

Next, the variations in the switching parameters of the PSD (CoolMOS 47N50) for varying optical power levels are measured. First, turn-ON and turn-OFF delays, and rise and fall times of the PSD for varying optical power levels are plotted in Fig. 21, and then the time-domain snapshots are shown in Fig. 22. Three distinct test cases are considered and they are described as follows.

1) *ON-laser variation:* Power of the ON-laser is varied from 0.25 to 2 W and that of the OFF-laser is held constant at 1 W. This will result in a variation in $R_{\text{ON-OTPT}}$, while $R_{\text{OFF-OTPT}}$ remains constant. Therefore, primarily turn-ON dynamics can be controlled.
2) *OFF-laser variation:* In this case, power of the OFF-laser is varied from 0.25 to 2 W and that of the ON-laser is held constant at 1 W resulting in variation in the $R_{\text{OFF-OTPT}}$, while $R_{\text{ON-OTPT}}$ remains constant. Therefore, primarily turn-OFF dynamics can be controlled.
3) *ON-laser and OFF-laser variations:* In the more general case, power levels of both the ON-laser and OFF-laser are varied simultaneously with the ratio 1 : 1 from 0.25 to 2 W. This will result in variations in the values of $R_{\text{ON-OTPT}}$, as well as $R_{\text{OFF-OTPT}}$. Both turn-ON and turn-OFF dynamics can be controlled in this mode of operation.

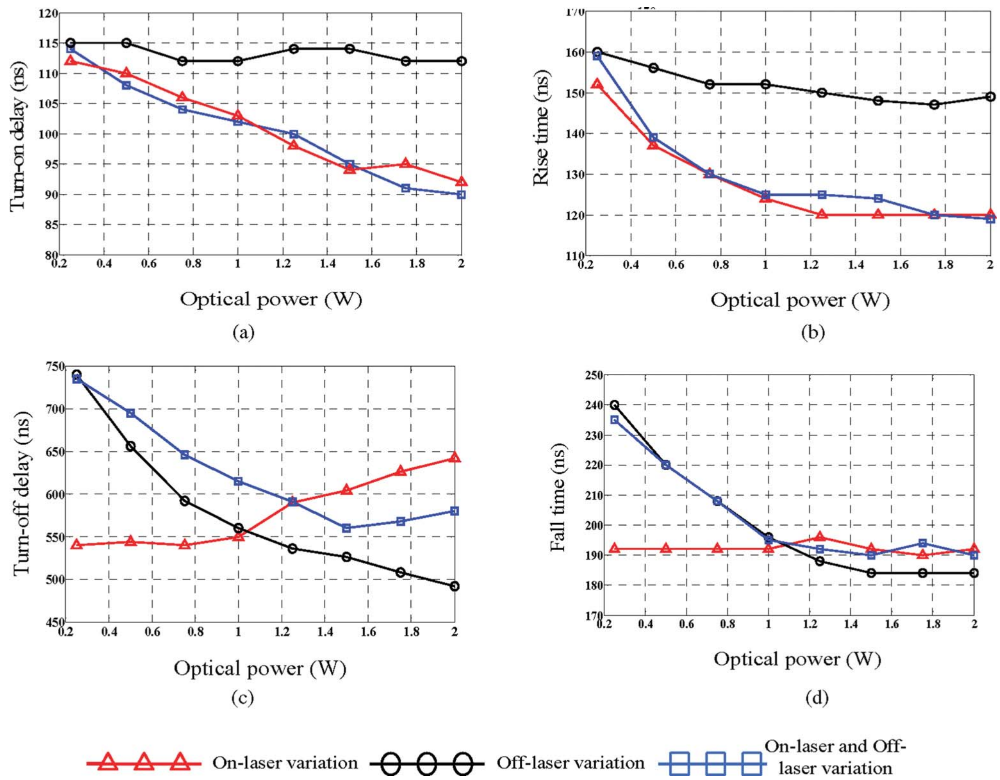

Fig. 21. Modulation of the (a) turn-ON delay, (b) rise time, (c) turn-OFF delay, and (d) fall time of the CoolMOS (part number 47N50) with varying optical power under the following conditions: $V_{\mathrm{Bias}} = 12$ V, $V_{\mathrm{High}} = 50$ V, $R_{\mathrm{load}} = 40\,\Omega$, frequency $= 30$ kHz, and duty cycle $= 50\%$.

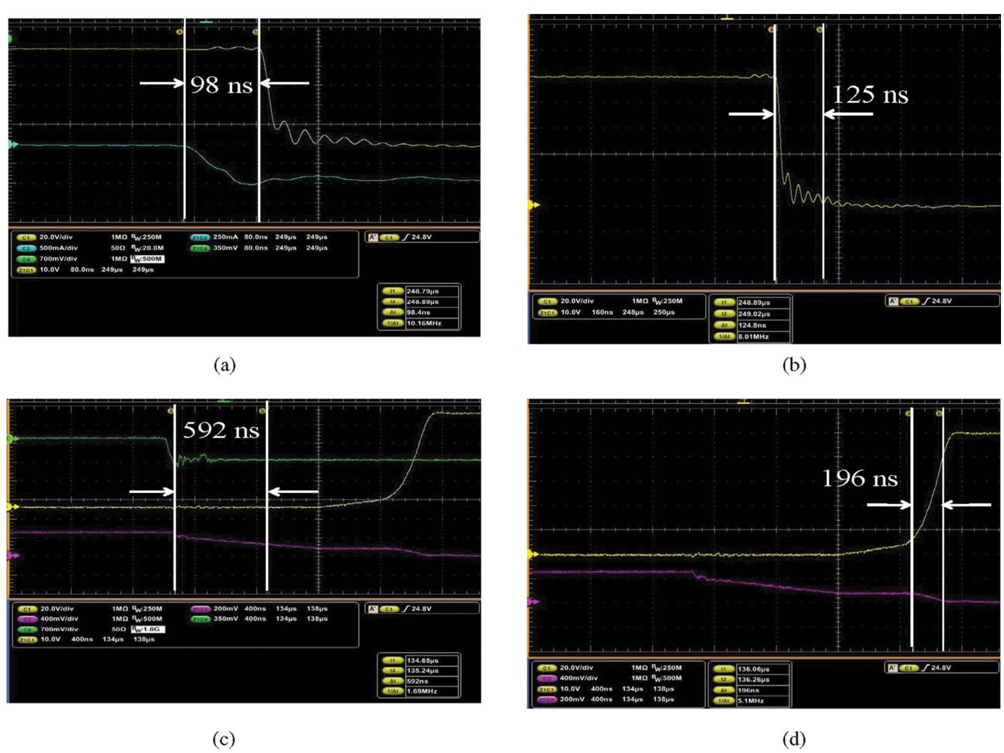

Fig. 22. Time-domain snapshots of (a) turn-ON delay (98.4 ns), (b) rise time (124.8 ns), (c) turn-OFF delay (592 ns), and (d) fall time (196 ns) of the CoolMOS (part number 47N50) obtained under the following conditions: $V_{\mathrm{Bias}} = 12$ V, $V_{\mathrm{High}} = 50$ V, $R_{\mathrm{load}} = 40\,\Omega$, frequency $= 30$ kHz, and duty cycle $= 50\%$. (a) Top trace is the voltage across the CoolMOS and the bottom trace is the output current signal of the ON-laser driver. (b) Only trace is the voltage across the CoolMOS. (c) Topmost trace is the output current signal of the OFF-laser driver, next trace is the voltage across the CoolMOS, and bottom trace is the gate-to-source voltage of the CoolMOS. (d) Top trace is the voltage across the CoolMOS and the bottom trace is the gate-to-source voltage of the CoolMOS. The laser-driver current signal is measured through an internal current monitor of the laser-driver and is of negative polarity.

It is seen from Fig. 21 that rise time and turn-ON delay decrease with the variation in the ON-laser power or with the simultaneous variation in the ON-laser and OFF-laser powers, whereas they are not much affected by the OFF-laser power variation. In a complimentary manner, fall time and turn-OFF delay decrease with the variation in the OFF-laser power or with the simultaneous variation in the ON-laser and OFF-laser powers, whereas they are not much affected by the sole variation in the ON-laser power. However, all four switching parameters (i.e., rise time, fall time, turn-ON delay, and turn-OFF delay) are affected by simultaneous variations in the ON-laser and OFF-laser power levels. Time-domain snapshots of the turn-ON and turn-OFF delays and rise and fall times are shown in Fig. 22.

So far, only the PSD switching dynamics modulation is discussed. Because OTPT is a single-stage device incorporating dual functions of optical-to-electrical conversion and gate driving, the delay between the control signal and the onset of the PSD switching is likely to be the least for the OAGC approach as compared to existing optical isolation techniques. This hypothesis is experimentally validated. Optoisolator gate driver HCPL 3101 and optical receiver/transmitter (HP T-1521/R-2521, 5 MBOD optical data link), along with TC4420 gate driver, are used for benchmarking. For all of the cases, the delay is measured between the control input signal and the onset of change in the voltage across the PSD. The comparative results are shown in Fig. 23. The optoisolator gate driver displays largest delay ($\sim$1.12 μs) followed by optical receiver/transmitter pair ($\sim$440 ns), whereas the optical triggering by OTPT gives least delay ($\sim$132 ns). Moreover, this delay can be controlled by varying the optical power, as evident in Fig. 21. For the other two cases, the delay is preset by the gate driver IC, fixed gate resistance, and fixed delay of the optical-to-electrical conversion circuit.

The scalability of the OAGC concept to other PSDs is further demonstrated. The OTPT(s) are coupled, in turn, to Si-based power MOSFET (CoolMOS part number 47N50), Si-based IGBT (IRG4CC50), 600-V SiC-based normally-ON VJFET (obtained from SiCED AG, Germany), and 600-V SiC-based DMOSFET (obtained from Cree, Inc., USA) following identical circuit arrangement, as shown in Fig. 3(a). Nominal switching operation with identical optical power is tested and the results are shown in Fig. 24. For all the PSD types, the voltage waveform of the PSD follows the optical signal closely over a wide range of switching frequency and pulsewidth.

C. Impact of the OAGC on Converter-Performance Parameters

For experimental characterization of the modulation of the converter-performance parameters, a dc/dc buck converter is built. The details of the experimental setup and parameters are given in Table II. The circuit schematic is illustrated in Fig. 25. Two optical sources are used to generate complimentary triggering signals for achieving controllability of the turn-ON and turn-OFF dynamics. Identical test cases (ON-laser variation, OFF-laser variation, and ON-laser and OFF-laser variations) are considered.

The variation in the power-conversion efficiency of the converter with varying optical power is plotted in Fig. 26. An initial sharp increment in the power-conversion efficiency is followed by a gradually saturating behavior. This shape is almost reciprocal to that observed in the variations of the OTPT ON-resistance,

(a) (b) (c)

Fig. 23. Demonstration of lower turn-ON delay as compared to other optical-isolation techniques under following experimental conditions: $V_{\rm Bias} = 12$ V, $V_{\rm High} = 300$ V, duty cycle = 10%, and frequency = 10 kHz. Turn-ON delay values are found to be, respectively, (a) 1.12 μs with optoisolator, (b) 440 ns with the fiber-optic transmitter–receiver, and (c) 132 ns with the OTPT. For all of the cases, the top trace denotes the voltage across the CoolMOS (part number 47N50) and the bottom trace denotes the corresponding control signal. For the optoisolator-based scheme, the control signal is the electrical logic signal, while for the fiber-optic transmitter–receiver scheme, the control signal is the electrical logic signal at the input of optical transmitter. Finally, for the OTPT-based scheme, the control signal is the laser driver current signal.

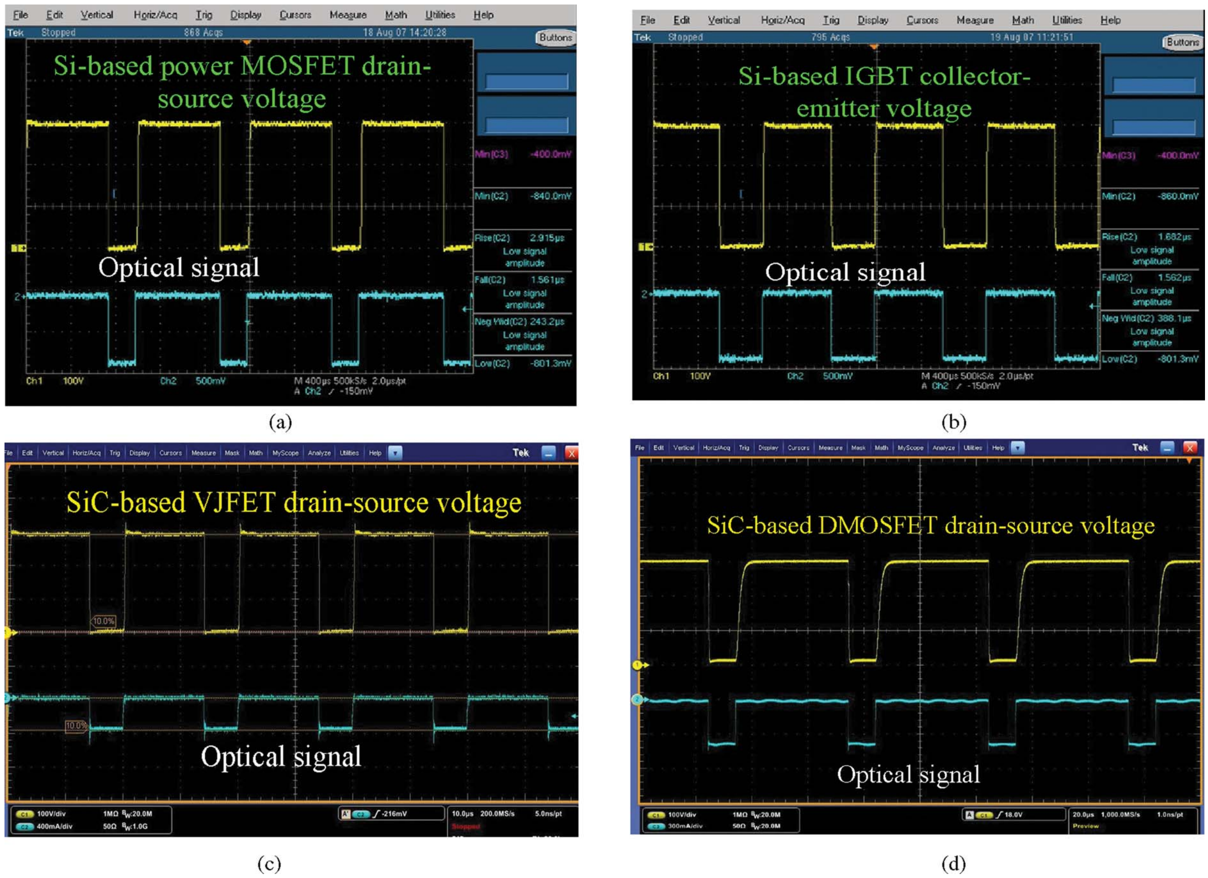

Fig. 24. Nominal switching operation for the OTPT(s) coupled to different types of PSDs. (a) Si-based power MOSFET (CoolMOS part number 47N50). (b) Si-based IGBT (IRG4CC50). (c) Six hundred volts normally-ON SiC-based VJFET. (d) Six hundred volts SiC-based DMOSFET. The dynamics of the SiC DMOSFET is comparatively slower due to the high input capacitance of the device and is not attributed to the OTPT.

TABLE II
DETAILS OF THE EXPERIMENTAL SETUP FOR THE BUCK CONVERTER

Input voltage (V_{in})	40 V	Logic bias (V_{Bias})	12 V
Output load (R_{load})	8 ohm	Filter inductor	200 µH
Switching frequency	100 kHz	Filter capacitor	330 µF
Duty ratio	50%	Diode	DGSS20-06CC
Laser wavelength	808 nm	Power MOSFET (PSD)	Part # IRF530

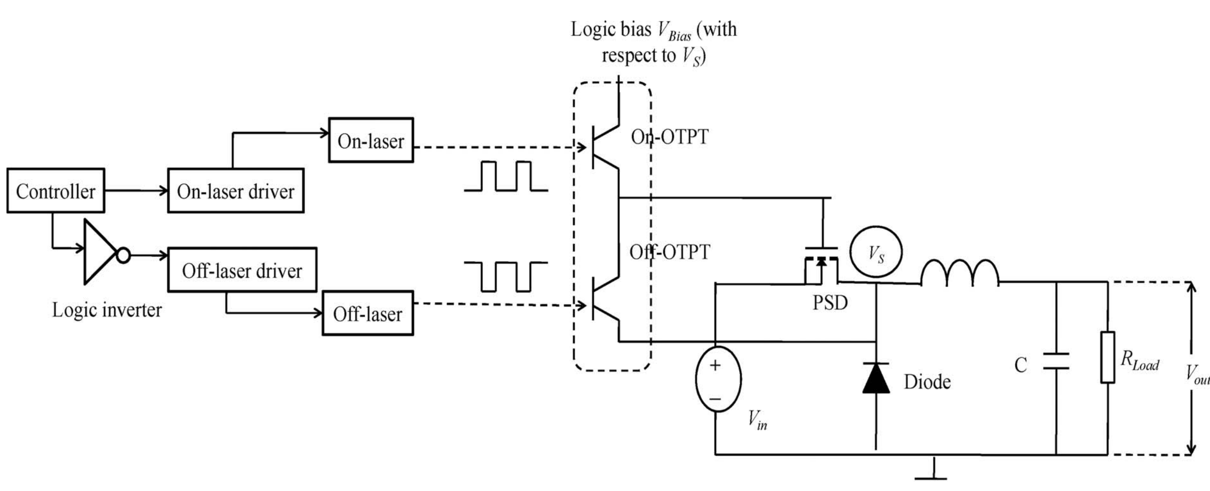

Fig. 25. Circuit schematic of the OAGC-based buck converter.

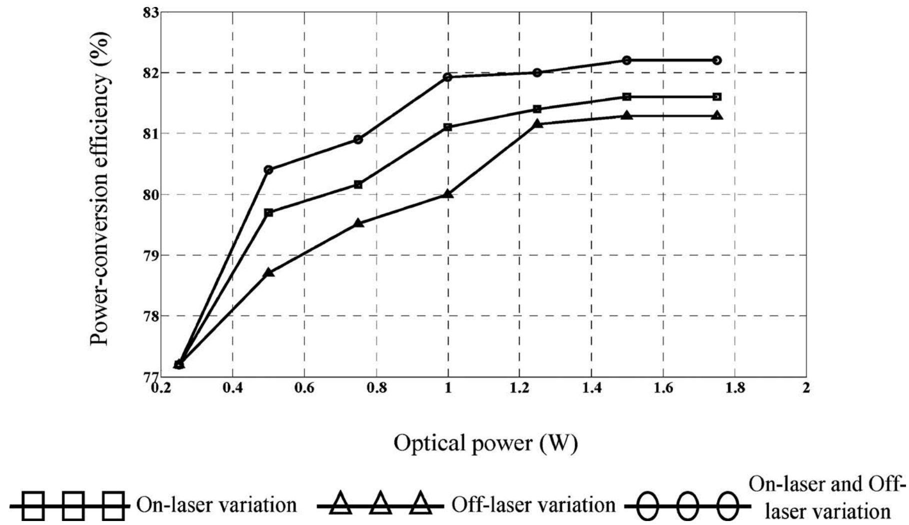

Fig. 26. Power-conversion efficiency of the buck converter (in Fig. 25) with varying OTPT optical power and under the following conditions: $V_{\mathrm{in}} = 20$ V, frequency $= 100$ kHz, duty cycle $= 50\%$, $R_{\mathrm{load}} = 2\ \Omega$, and $P_{\mathrm{load}} = 50$ W.

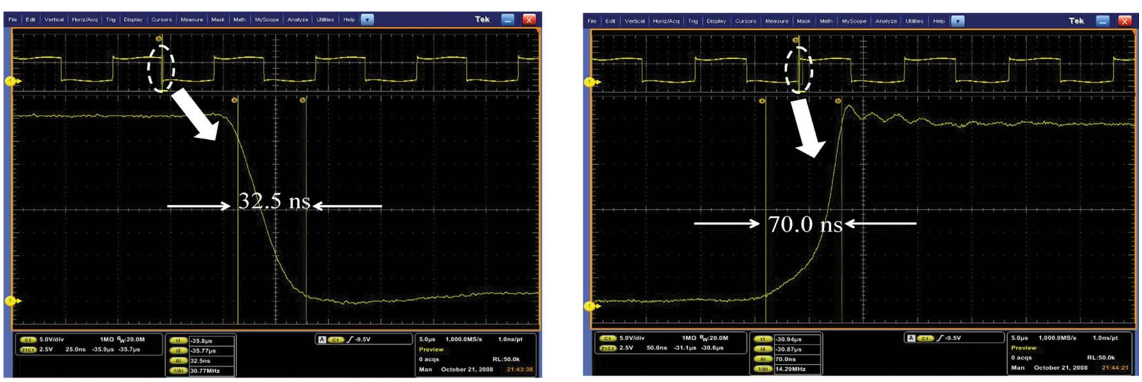

(a) (b)

Fig. 27. Representative time-domain snapshot showing (a) the rise time and (b) the fall time of the voltage waveform across the power MOSFET in the buck converter during nominal operation. Horizontal scales: (a) 25 ns/div and (b) 50 ns/div. Vertical scales: [(a) and (b)] 2.5 V/div.

which is consistent with (9). While the peak efficiency in absolute terms is $\sim$82.5%, it is noteworthy that the key idea behind this converter-based study is to demonstrate the applicability of the OAGC scheme at a system level. The absolute value of the efficiency and its range of modulation can change depending on the topology, components type, technology and ratings, and converter operating conditions. Nevertheless, the dynamic controllability of the efficiency with the optical power modulation can be demonstrated in most cases, because fundamentally, the OAGC modulates the switching loss.

Assuming a linear change in the voltage/current across the PSD during switching, the dv/dt (or di/dt) stress can be calculated, approximately, by dividing the peak voltage (or current) by the rise/fall times. Because voltage and current change sharply during turn-ON and turn-OFF instants, the dv/dt and di/dt stresses are measured for both turn ON and turn OFF. Representative time-domain results (rise time and fall time of the voltage across the PSD) are shown in Fig. 27, and dv/dt and di/dt stresses are plotted in Fig. 28.

Next, the modulation of the EM noise spectrum is studied experimentally (as illustrated in Fig. 29). Conducted common-mode noise, measured using the input current waveform of the converter, is chosen for this purpose. Agilent spectrum analyzer 4395 A is used to capture the frequency-domain representation of the input current waveform. High-bandwidth, Hall-sensor current probe is placed around the input cable and the output of the probe is connected to the spectrum analyzer through 50 Ω BNC termination (see Fig. 29). Analyzer output is connected to a PC and the spectrum data is directly captured through a general-purpose interface bus (GPIB)/universal serial bus (USB) interface. Generally, for conducted-noise measurement, one commonly used frequency band is 10 kHz–5 MHz [31]. Accordingly, the low- and high-frequency limits are set at 10 kHz and 5 MHz, respectively, with a 1-kHz resolution. Results are shown in Fig. 30 for two distinct optical-power levels. The envelope of the spectrum is drawn for the second case (2.0 W) by joining the peaks of the magnitudes. Exactly the same envelope, when superimposed on the other one (0.5 W), illustrates

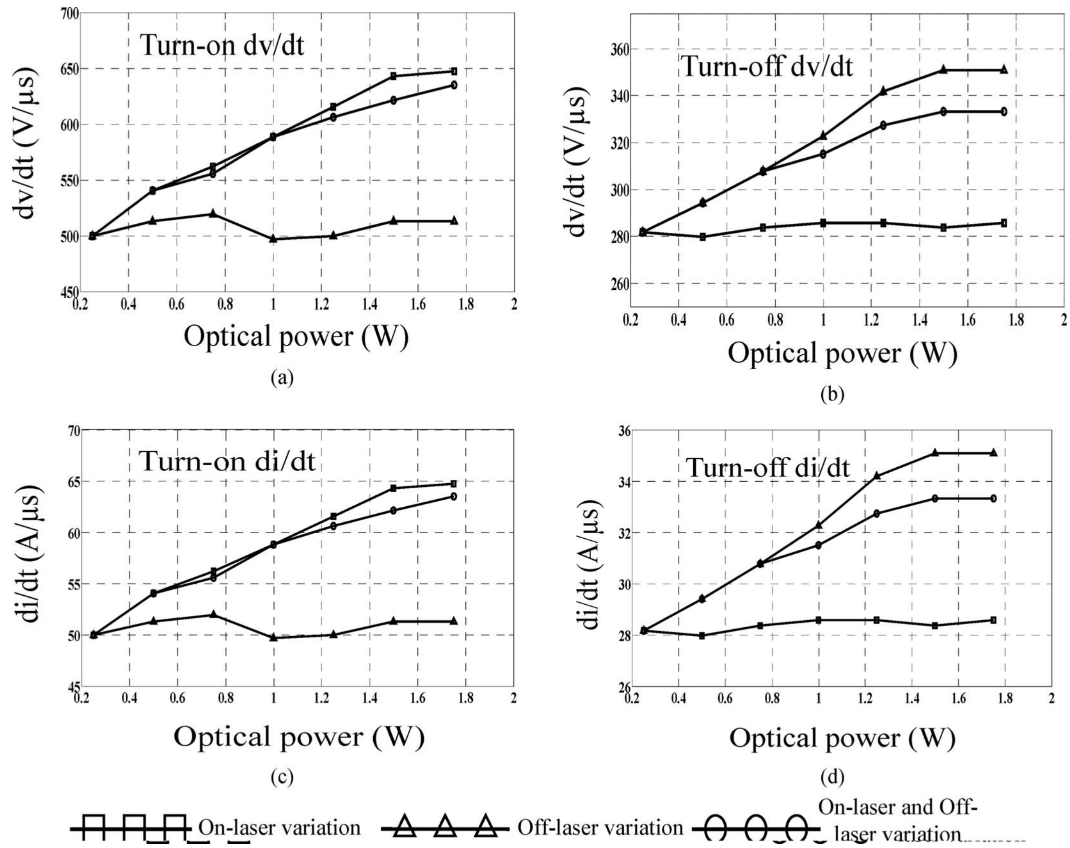

Fig. 28. Modulation of dv/dt and di/dt stresses of the PSD during turn-ON and turn-OFF with varying optical-power levels.

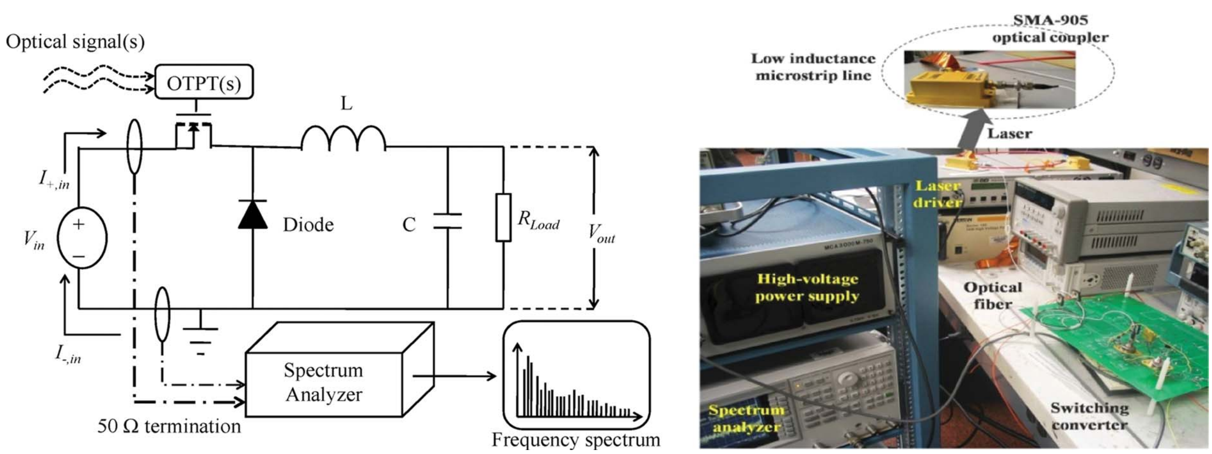

Fig. 29. Schematic and photograph of the experimental setup for studying the modulation of the EM-noise spectrum of the prototype buck converter.

the changes in the spectrum, which occurred due to a change in the optical intensity. Smaller optical power lowers the common-mode noise amplitudes in the high-frequency range by slowing down the switching speed of the power MOSFET.

The effect of the variation in optical power is most pronounced at high frequency (>2 MHz for this case) since the optical power affects the PSD rise and fall times, which are of the order of tens of nanoseconds. By controlling EM-noise without using external EMI filter, the present approach may preclude the need for changing converter complexity and dynamics. Moreover, the results reported in this paper provide a concept demonstration at low power levels. For high-power and high-frequency converters (e.g., using SiC devices), the absolute values of the EM noise reduction is expected to be significantly higher.

The optimization framework (see Section II) is used to calculate the objective function and determine the optimal optical power level. Total loss is extracted from the experimentally measured efficiency values using (13) and is plotted in Fig. 31. Data corresponding to Figs. 28 and 31 are used to calculate the objective function. Following three test conditions (i.e.,

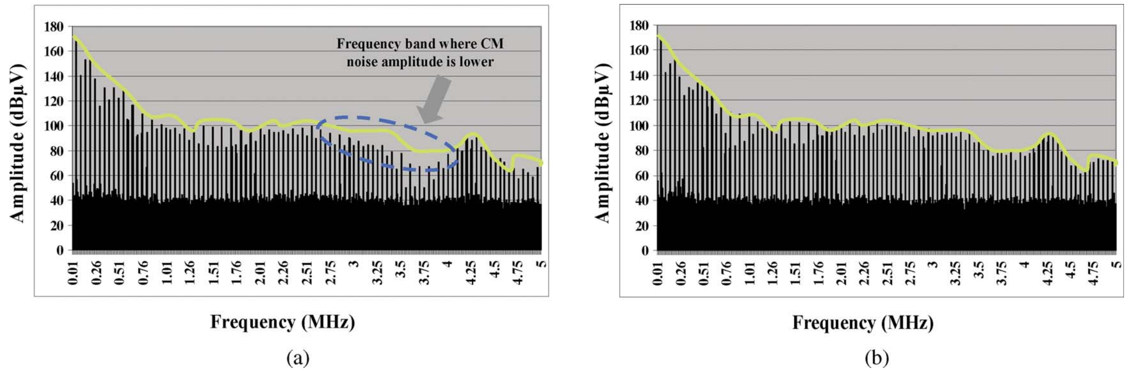

Fig. 30. Buck converter input-current-noise spectrum (10 kHz–5 MHz at 1 kHz resolution) for optical-power levels of (a) 500 mW and (b) 2.0 W. The faded line (touching the amplitude peaks) shows the exact same envelope to illustrate the effect of the two different optical-power levels.

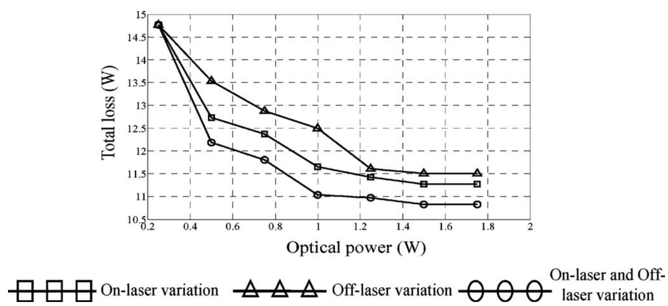

Fig. 31. Total loss for the buck converter (shown in Fig. 25), with varying optical power as extracted from the experimentally measured power-conversion efficiency values.

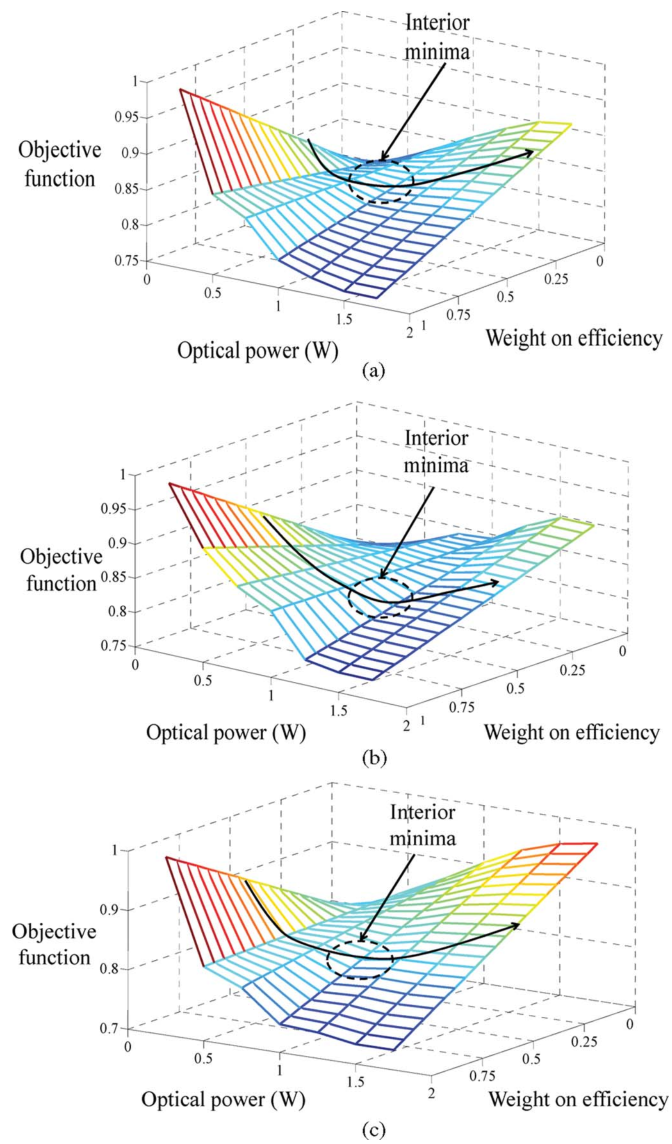

Fig. 32. Experimentally measured objective function and its minima for (a) ON-laser variation, (b) OFF-laser variation, and (c) ON-laser and OFF-laser variations.

ON-laser variation, OFF-laser variation, and ON-laser and OFF-laser variations), corresponding objective function values are shown in Fig. 32(a)–(c). The minimum point of the objective function, which corresponds to the optimal optical intensity, can be observed for all of the three cases.

It can also be seen from Fig. 32 that the optimum point occurs at different optical power levels for different distribution of the weights on power-conversion efficiency. In Fig. 33, the optimum optical-power level is plotted against the weight on efficiency for all three cases. It is observed that there exists a limited range of optimization (corresponding to a limited range of weight on the power-conversion efficiency) within which the objective function curve exhibits an interior minima. Outside this range, the minimum value of the objective function lies at the boundary of optical-intensity range. For very small weight on the power-conversion efficiency, the minimum point of the objective function lies on the left-hand side boundary of the optical-intensity range. Physically, this corresponds to very low optical power leading to poor efficiency, but much reduced PSD stress (because of the slow switching dynamics of the PSD). On the other hand, for a very small weight on the PSD stress, the minimum point of the objective function lies on the right-hand side boundary of the optical-intensity range. Physically, this corresponds to high optical power leading to higher efficiency and enhanced PSD stress (because of fast switching dynamics

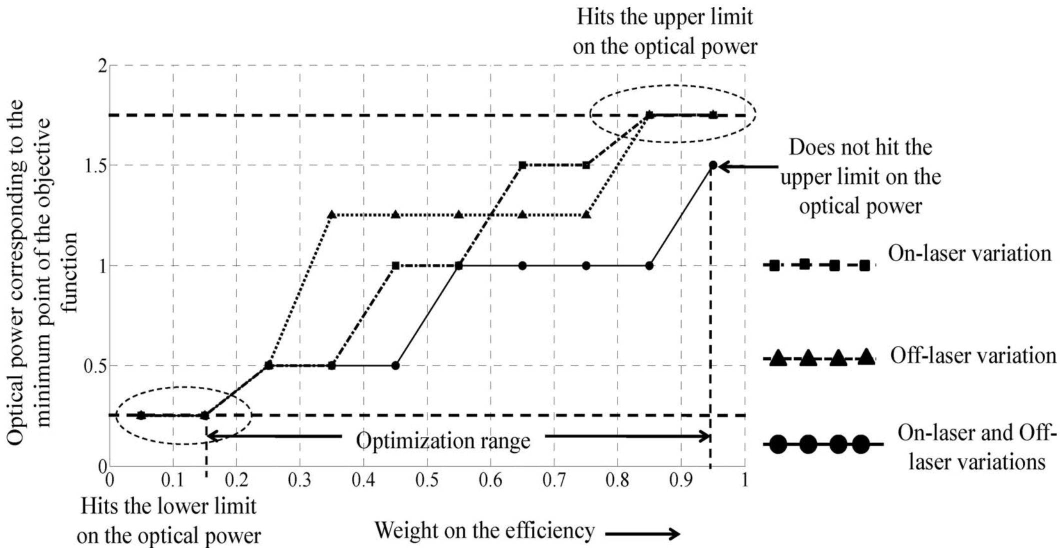

Fig. 33. Experimentally measured optical power at which the objective function [described by (16)] attains minima with varying weight on power-conversion efficiency. It can be observed that the range of optimization is largest for the scheme with turn-ON and turn-OFF controllability (ON-laser and OFF-laser variations).

of the PSD). It is also observed from Fig. 33 that this range of optimization is maximum for the case when the intensities of both the ON-laser and the OFF-laser vary simultaneously.

V. Summary and Conclusion

Control of switching loss (and hence, power-conversion efficiency), dv/dt and di/dt stresses, and EM-noise emission (referred to as the converter-performance parameters) of a power converter comprising one or more PSDs at the device level has attained significance in the context of next-generation rapid-response, high-frequency, energy-efficient, and robust power-electronics and pulsed-power/pulsed-load systems. In this regard, this paper outlines a novel OAGC concept that enables the dynamic control of a PSD using an OTPT, which modulates the excitation of the PSD.

OAGC differs from the electrical AGC in several aspects. First, OAGC reduces switching initiation delay due to direct photogeneration and reduced stages in the driver. Second, OAGC can be realized by modulating optical intensity, as well as wavelength, both of which can enable conductivity modulation of the OTPT [24]. Third, OAGC enables integration of optical isolation and converter-performance control at device level in a single framework. Finally, with reference to high-ambient-temperature power electronics using wide-bandgap PSDs, OAGC can enable integration of the driver and the PSD by optically compensating the temperature-induced drift in the PSD switching dynamics. A preliminary study in this regard has been done and the GaAs OTPT is shown to work successfully up to 200 °C temperature along with an SiC DMOSFET. Details of this investigation are presented in [32].

OAGC can potentially be realized in a single monolithic device by integrating the OTPT and the PSD. Integrated optical switch in the form of light-triggered thyristor (LTT) [20] has been demonstrated. While the turn-ON of the LTT is initiated with small optical power, the turn-OFF dynamics, unlike OAGC, is not optically controlled. Further research needs to be carried out to assess the tradeoff between effectiveness of an integrated approach and cost, complexity, and reliability of fabrication. In contrast to the integrated approach, a key advantage of a hybrid scheme is scalability with respect to the PSD rating, material, or structural variations, as demonstrated in this paper. For instance, GaAs-based OTPT can couple with existing Si- or SiC-based PSDs using off-the-shelf and cost-effective long-wavelength (800–850 nm) optical sources and drivers.

We further outline a mechanism for controlling converter-performance parameters by varying the triggering optical intensity of the OTPT. The fundamental link in this process is identified to be the ON-resistance of the OTPT, which is optically modulated to control the gate excitation of the PSD. Experimental results on converter-performance parameters as a function of OTPT optical intensity demonstrate this correlation. It is also gathered from the parametric studies and analysis that sensitivity of the ON-resistance of the OTPT along with its quantum efficiency are key design factors from both cost and application standpoints. The choice of a material (such as GaAs) with high optical-absorption efficiency, optimal refractive index of the OTPT antireflecting passivation layer, and the wavelength of optical excitation are important design parameters.

With regard to the PSD switching dynamics modulation, three distinct types of OAGC mechanisms were explored for controlling the turn-ON/turn-OFF/and both turn-ON and turn-OFF dynamics. Because there exists a mutually contrasting dependence of PSD dv/dt and di/dt stresses, and switching loss (or power-conversion efficiency) on optical intensity of the OTPT, the necessity of joint optimization is realized and experimentally explored. The range of this optimization depends on the weights placed on power-conversion efficiency and PSD dv/dt and di/dt stresses, and is maximum for the OAGC scheme with both turn-ON and turn-OFF controllability. Finally, with reference to the EM-noise modulation, the effect of OTPT optical intensity is found to be more pronounced in the high-frequency region because the variation in the optical intensity primarily affects the dynamics of the PSD switching-edge transition, which is on the order of nanoseconds.

APPENDIX I

FUNCTIONAL FORMS FOR OPTICAL-INTENSITY-DEPENDENT ON-RESISTANCE AND RISE TIME OF THE OTPT

The relation between the OTPT ON-resistance and the optical intensity of the OTPT ($P_{\rm OTPT}$) is given by [21]

$$\begin{aligned} R_{\rm OTPT} &= f_1(P_{\rm OTPT}) \\ &= \frac{K_1}{K_1' P_{\rm OTPT} + K_1''} + \frac{K_2}{K_2' P_{\rm OTPT} + K_2''} \end{aligned} \tag{A1}$$

where $K_1, K_2, K_1', K_1'', K_2'$, and K_2'' are constants depending on the material (GaAs in this particular case) properties, and device design parameters (e.g., doping densities, dimensions of different regions in the device, and the active die area).

The relation between the OTPT rise time and its optical-intensity input is given by [21]

$$\begin{aligned} t_{\rm rise,OTPT} &= f_2(P_{\rm OTPT}) \\ &= \tau_{nH}\left[\ln\left(\frac{M_1 P_{\rm OTPT} + M_2}{M_3 P_{\rm OTPT}}\right)^{M_4} + \frac{(M_5 P_{\rm OTPT} + M_6)}{\sqrt{M_7 P_{\rm OTPT}^2 + M_8}}\right. \\ &\qquad \left.\times \ln\left(\frac{M_9 P_{\rm OTPT} + M_{10} - \sqrt{M_7 P_{\rm OTPT}^2 + M_8}}{M_9 P_{\rm OTPT} + M_{10} + \sqrt{M_7 P_{\rm OTPT}^2 + M_8}}\right)\right] \end{aligned} \tag{A2}$$

where τ_{nH} is the minority carrier lifetime and M_j ($\forall j = 1, 2, \ldots, 10$) are different constants that depend on the material (GaAs for this particular case) properties, particular device design parameters, wavelength of optical signal, and circuit load conditions. It is to be noted that these relations are valid under isothermal condition (i.e., the temperature change inside the device caused by photogeneration is neglected) and under the assumption that photogeneration does not change the parameters of carrier-transport dynamics (such as mobility, diffusion coefficient, or Shockley–Read–Hall (SRH) lifetime) or the optical properties of the material (such as the optical-absorption coefficient).

APPENDIX II

AMPLITUDE OF THE HARMONIC COMPONENTS OF THE FREQUENCY SPECTRUM IN FIG. 6

The trapezoidal waveform in Fig. 6 can be described by the (A3), as shown at the bottom of this page.

For brevity of the mathematical expressions, the following quantities are defined:

$$X = dT + t_{\rm rise,PSD} \quad \text{and} \quad Y = dT + t_{\rm rise,PSD} + t_{\rm fall,PSD}. \tag{A4}$$

The magnitude of the nth harmonic of $f(t)$ can be obtained from the complex Fourier coefficient, which is defined by

$$|A_n| = |a_n - jb_n| = \sqrt{a_n^2 + b_n^2} \tag{A5}$$

where

$$\begin{aligned} a_n &= \frac{2}{T}\int_0^T f(t)\cos\left(\frac{2n\pi t}{T}\right)dt \quad \text{and} \\ b_n &= \frac{2}{T}\int_0^T f(t)\sin\left(\frac{2n\pi t}{T}\right)dt. \end{aligned} \tag{A6}$$

Using (A3) to deduce the limits of the integral, (A6) can be rewritten as

$$\begin{aligned} a_n &= \frac{2}{T}\left[\int_0^{t_{\rm rise,PSD}} V_{\rm in}\frac{t}{t_{\rm rise,PSD}}\cos\left(\frac{2n\pi t}{T}\right)dt \right.\\ &\quad + \int_{t_{\rm rise,PSD}}^{X} V_{\rm in}\cos\left(\frac{2n\pi t}{T}\right)dt \\ &\quad \left. + \int_X^Y V_{\rm in}\left(1 - \frac{t-Y}{t_{\rm fall,PSD}}\right)\cos\left(\frac{2n\pi t}{T}\right)dt\right] \\ b_n &= \frac{2}{T}\left[\int_0^{t_{\rm rise,PSD}} V_{\rm in}\frac{t}{t_{\rm rise,PSD}}\sin\left(\frac{2n\pi t}{T}\right)dt \right.\\ &\quad + \int_{t_{\rm rise,PSD}}^{X} V_{\rm in}\sin\left(\frac{2n\pi t}{T}\right)dt \\ &\quad \left. + \int_X^Y V_{\rm in}\left(1 - \frac{t-Y}{t_{\rm fall,PSD}}\right)\sin\left(\frac{2n\pi t}{T}\right)dt\right]. \end{aligned} \tag{A7}$$

$$f(t) = \begin{cases} V_{\rm in}\dfrac{t}{t_r}, & 0 \le t \le t_{\rm rise,PSD} \\ V_{\rm in}, & t_r < t \le dT + t_{\rm rise,PSD} \\ V_{\rm in}\left[1 - \dfrac{t - (dT + t_{\rm rise,PSD})}{t_{\rm fall,PSD}}\right], & dT + t_{\rm rise,PSD} < t \le dT + t_{\rm rise,PSD} + t_{\rm fall,PSD} \\ 0, & dT + t_{\rm rise,PSD} + t_{\rm fall,PSD} < t \le T. \end{cases} \tag{A3}$$

Evaluations of the integrals in (A7) yield the following expressions for a_n and b_n:

$$a_n = g_1(t_{\mathrm{rise,PSD}}, t_{\mathrm{fall,PSD}}) = \frac{2V_{\mathrm{in}}}{T} \times \Bigg[\frac{1}{k^2 t_{\mathrm{rise,PSD}}}(\cos(kt_{\mathrm{rise,PSD}}) + kt_{\mathrm{rise,PSD}}\sin(kt_{\mathrm{rise,PSD}}) - 1) + \frac{1}{k}(\sin(kX) - \sin(kt_{\mathrm{rise,PSD}})) + \frac{Y}{kt_{\mathrm{fall,PSD}}} \times (\sin(kY) - \sin(kX)) - \frac{1}{k^2 t_{\mathrm{fall,PSD}}}(\cos(kY) - \cos(kX) + kY\sin(kY) - kX\sin(kX))\Bigg] \tag{A8a}$$

$$b_n = g_2(t_{\mathrm{rise,PSD}}, t_{\mathrm{fall,PSD}}) = \frac{2V_{\mathrm{in}}}{T} \times \Bigg[\frac{1}{k^2 t_{\mathrm{rise,PSD}}}(\sin(kt_{\mathrm{rise,PSD}}) - kt_{\mathrm{rise,PSD}}\cos(kt_{\mathrm{rise,PSD}})) + \frac{1}{k}(\cos(kt_{\mathrm{rise,PSD}}) - \cos(kX)) + \frac{Y}{kt_{\mathrm{fall,PSD}}}(\cos(kX) - \cos(kY)) - \frac{1}{k^2 t_{\mathrm{fall,PSD}}}(\sin(kY) - \sin(kX) + kX\cos(kX) - kY\cos(kY))\Bigg]. \tag{A8b}$$

Acknowledgment

Any opinions, findings, conclusions, or recommendations expressed herein are those of the authors and do not necessarily reflect the views of the Office of Naval Research or the National Science Foundation.

References

[1] W. H. Sew, Q. Li, M. G. Stewart, K. Walker, and C. Piner, "Measurement of electromagnetic emissions from FACTS equipment operational within substations—Part I," *IEEE Trans. Power Del.*, vol. 20, no. 2, pp. 1775–1881, Apr. 2005.
[2] S. K. Mazumder and T. Sarkar, "Optical modulation for high power systems: Potential for electromagnetic-emission, loss, and stress control by switching dynamics variation of power semiconductor devices," in *Proc. IEEE Energy 2030 Conf.*, 2008, pp. 1–8.
[3] P. Lefranc and D. Bergogne. (2007). State of the art of dv/dt and di/dt control of insulated gate power switches. presented at the Power Supply Energy Manag. Defense Appl., Brussels, Belgium [Online]. Available: http://hal.archives-ouvertes.fr/docs/00/21/42/11/PDF/lefranc_bergogne_iap1_2007.pdf
[4] E. Y. Y. Ho, Y. Li, J. Honda, D. C. Tam, T. Takahashi, and R. P. Verdes, "Global closed loop control system with dv/dt control and EMI/switching loss reduction," U.S. Patent 7 061 195, 2006.
[5] T. Ericsen, N. Hingorani, and Y. Khersonsky, "Power electronics and future marine electrical systems," *IEEE Trans. Ind. Appl.*, vol. 42, no. 1, pp. 155–163, Jan./Feb. 2006.
[6] J. D. Kagerbauer and T. M. Jahns, "Development of an active dv/dt control algorithm for reducing inverter conducted EMI with minimal impact on switching losses," in *Proc. IEEE Power Electron. Spec. Conf.*, 2007, pp. 894–900.
[7] M. R. Doyle, D. J. Samuel, T. Conway, and R. R. Klimowski, "Electromagnetic aircraft launch system-EMALS," *IEEE Trans. Magn.*, vol. 31, no. 1, pp. 528–533, Jan. 1995.
[8] J. R. Todd, "Direct optical control: A lightweight backup consideration," in *Proc. IEEE Nat. Aerosp. Electron. Conf.*, 1992, vol. 2, pp. 456–463.
[9] S. K. Mazumder and T. Sarkar, "Optically-triggered power transistor (OTPT) for fly-by-light (FBL)/EMI susceptible power electronics," in *Proc. IEEE Power Electron. Spec. Conf.*, 2006, pp. 1–8, Plenary Paper.
[10] S. K. Mazumder and T. Sarkar, "SiC-based optically-gated high-power solid-state switch for pulsed-power application," *J. Mater. Sci. Forum*, vol. 600–603, pp. 1195–1198, 2008.
[11] F.-J. Niedernostheide, H.-J. Schulze, H.-P. Felsl, T. Laska, U. Kellner-Werdehausen, and J. Lutz, "Thyristors and IGBTs with integrated self-protection functions," *IET Trans. Circuits, Devices, Syst.*, vol. 1, no. 5, pp. 315–320, 2007.
[12] J. A. Weimer, "Electrical power technology for the more electric aircraft," in *Proc. IEEE Digital Avionics Syst. Conf.*, 1993, pp. 445–450.
[13] A. Garcia, I. Cusido, J. A. Rosero, J. A. Ortega, and L. Romeral, "Reliable electro-mechanical actuators in aircraft," *IEEE Aerosp. Electron. Syst. Mag.*, vol. 23, no. 8, pp. 19–25, Aug. 2008.
[14] A. Hefner, S. H. Ryu, B. Hull, D. Berning, C. Hood, J. M. Ortiz-Rodriguez, A. Rivera-Lopez, T. Duong, A. Akuffo, and M. Hernandez-Mora, "Recent advances in high-voltage, high-frequency silicon-carbide power devices," in *Proc. IEEE Ind. Appl. Soc. Conf.*, 2006, pp. 330–337.
[15] S. Park and T. M. Jahns, "Flexible dv/dt and di/dt control method for insulated gate power switches," *IEEE Trans. Ind. Appl.*, vol. 39, no. 3, pp. 657–664, May/Jun. 2003.
[16] H. Wang, A. Q. Huang, and F. Wang, "Development of a scalable power semiconductor switch (SPSS)," *IEEE Trans. Power Electron.*, vol. 22, no. 2, pp. 364–373, Mar. 2007.
[17] P. J. Grvobic, "An IGBT gate driver for feed-forward control of turn-on losses and reverse recovery current," *IEEE Trans. Power Electron.*, vol. 23, no. 2, pp. 643–652, Mar. 2008.
[18] P. Bhadri, D. Sukumaran, K. Ye, S. Dasgupta, E. Guliants, and F. R. Beyette, Jr., "Design of a smart optically controlled high power switch for fly-by-light applications," in *Proc. IEEE Midwest Symp. Circuits Syst.*, 2001, vol. 1, pp. 401–404.
[19] O. S. F. Zucker, "Isolated control apparatus incorporating light-controlled power semiconductors," U.S. Patent 7 296 753, Nov. 2007.
[20] F. J. Niedernostheide, H. J. Schulzea, J. Dormb, U. Kellner-Werdehausenb, and D. Westerholtb, "Light-triggered thyristors with integrated protection functions," in *Proc. Int. Symp. Power Semicond. Devices ICs*, 2000, pp. 267–270.
[21] T. Sarkar and S. K. Mazumder, "Dynamic power density, wavelength, and switching time modulation of optically-triggered power transistor (OTPT) performance parameters," *Microelectron. J.*, vol. 38, pp. 285–298, 2007.
[22] V. Benda, J. Gowar, and D. A. Grant, *Power Semiconductor Devices*. West Sussex, U.K.: Wiley, 1999.
[23] N. Mohan, T. Undeland, and W. P. Robbins, *Power Electronics: Converters, Applications, and Design*. Hoboken, NJ: Wiley, 2003.
[24] L. Tihanyi, *Electromagnetic Compatibility in Power Electronics*. Piscataway, NJ: IEEE Press, 1995.
[25] R. Thomas, F. Li, and C. Garrett, "Prediction of radiated EMI from high frequency power converters," in *Proc. Int. Conf. Power Electron. Variable Speed Drives*, 2000, pp. 80–85.
[26] B. Audone, "Graphical harmonic analysis," *IEEE Trans. Electromagn. Compat.*, vol. EMC-15, no. 2, pp. 72–74, May 1973.
[27] X. Pei, K. Zhan, Y. Kang, and J. Chen, "Analytical estimation of common mode conducted EMI in PWM inverter," in *Proc. IEEE Ind. Appl. Soc. Conf.*, 2004, vol. 4, pp. 2651–2656.
[28] H. J. Keisler, *Elementary Calculus: An Infinitesimal Approach*. Boston, MA: Prindle, Weber & Schmidt, 1986.
[29] M. Brozel and G. Stillman, *Properties of Gallium Arsenide*. Chicago, IL: The Institution of Engineering and Technology, INSPEC, 1986.
[30] F. M. Dickey, S. C. Holswade, and D. L. Shealy, *Laser Beam Shaping Applications*. Boca Raton, FL: CRC Press, 2005.
[31] G. L. Skibinski, R. J. Kerkman, and D. Schlegel, "EMI emissions of modern PWM AC drives," *IEEE Ind. Appl. Mag.*, vol. 5, no. 6, pp. 47–81, Nov./Dec. 1999.
[32] S. K. Mazumder and T. Sarkar, "Optically-activated gate control (OAGC) for the next-generation SiC-based power electronics devices and applications," in *Proc. IEEE Energy Convers. Conf. Expo.*, 2009, pp. 2285–2292.
[33] S. K. Mazumder and T. Sarkar, "Optically-modulated active gate control for switching electrical power conversion systems," in *Proc. IEEE Electr. Ship Technol. Symp.*, Baltimore, MD, 2009, pp. 326–333.

Sudip K. Mazumder (SM'02) received the B.E. degree from the University of Delhi, India, in 1989, the M.S. degree from Rensselaer Polytechnic Institute, Troy, New York, in 1993 and the Ph.D. degree from Virginia Tech., in 2001.

He is the Director of the Laboratory for Energy and Switching-Electronics Systems, and a Professor in the Department of Electrical and Computer Engineering, University of Illinois, Chicago. He has more than 15 years of professional experience. He was at R&D and design positions in leading industrial organizations. His current research interests include interactive power electronics/power networks, renewable and alternative energy systems, photonically triggered and wide-bandgap-based power semiconductor devices, and applied technologies.

Dr. Mazumder was the first Editor-in-Chief of the *International Journal of Power Management Electronics* (now called *Advances in Power Electronics*) between 2006 to 2009. He has been an Associate Editor of the IEEE TRANSACTIONS ON INDUSTRIAL ELECTRONICS, IEEE TRANSACTIONS ON AEROSPACE AND ELECTRONIC SYSTEMS, and IEEE TRANSACTIONS ON POWER ELECTRONICS since 2003, 2008, and 2009, respectively. He was the Co-Chair of the IEEE Power Electronics Technical Committee on Sustainable Energy Systems. He was the Vice Chair of the Technical Program Committee of 2010 IEEE Energy Conversion Conference and Exposition. He was the Chair of the Student/Industry Coordination Activities for 2009 and 2010 IEEE Energy Conversion Congress and Exposition. He is also the Technical Program Committee Co-Chair of the 2010 IEEE International Symposium on Power Electronics for Distributed Generation Systems. He has been invited by the IEEE and the American Society of Mechanical Engineers, as well as multiple industries, federal agencies, national laboratories, and universities for several keynote, plenary, and invited lectures and presentations. He received the prestigious 2011 Teaching Recognition Program Award and the prestigious 2008 Faculty Research Award and the 2006 Diamond Award from the University of Illinois, Chicago for Outstanding Research Performance, the Office of Naval Research Young Investigator Award, the National Science Foundation CAREER Awards in 2005 and 2002, respectively, and the IEEE TRANSACTIONS ON POWER ELECTRONICS Prize Paper Award in 2002. He also co-received the 2007 IEEE Outstanding Student Paper Award at the IEEE International Conference on Advanced Information Networking and Applications.

Tirthajyoti Sarkar (S'03–M'10) received the B.Tech. degree (with President's Silver Medal Honor) from the Indian Institute of Technology (IIT) Kharagpur, Kharagpur, India, in 2003, and the Ph.D. degree in electrical engineering from the University of Illinois, Chicago, in 2009.

He worked as a Postdoctoral Research Associate in the Laboratory for Energy and Switching Electronics Systems, Department of Electrical and Computer Engineering, University of Illinois, in 2009 on projects related to optical-triggering of power semiconductor devices. Currently, he holds the position of Senior Device Engineer in the Device Design and Modeling Group of Fairchild Semiconductor and works in the area of low- and medium-voltage trench power MOSFET design and technology development. His research interests include power semiconductor devices, optical triggering for power electronics and semiconductor device simulation and modeling in general. He has authored or coauthored 13 peer-reviewed journal and international conference papers and an invited book chapter on optically-triggered power device.

Dr. Sarkar received "Joseph J. Suozzi Fellowship in Power Electronics" from the International Telecommunication Energy Conference and the IEEE Power Electronics Society in 2007 for his work on optical triggering in power electronics. He is a Life Member of the Semiconductor Society of India and has recently been inducted in the list of "Leading Scientists of the World, 2010" published by The International Biography Center, Cambridge, U.K.